Acta Geochim (2022) 41(2):165–184
https://doi.org/10.1007/s11631-021-00506-x

ORIGINAL ARTICLE

Application of low-temperature thermochronology on ore deposits preservation framework in South China: a review

Kang Min[1,2] · Jian-Feng Gao[1,2]

Received: 31 August 2021 / Revised: 18 October 2021 / Accepted: 19 October 2021 / Published online: 27 January 2022

Abstract South China can be divided into four metallogenic belts: The Middle-Lower Yangtze Metallogenic Belt (MLYB), Qinzhou-Hangzhou Metallogenic Belt (QHMB), Nanling Metallogenic Belt (NLMB), and Wuyi Metallogenic Belt (WYMB). The major mineralization in the four metallogenic belts is granite-related Cu–Au–Mo and porphyrite Fe-apatite, porphyry Cu (Au), and epithermal Pb–Zn–Ag, hydrothermal Cu–Au–Pb–Zn–Ag, and granite-related skarn-type and quartz-veins W–Sn, respectively. Low-temperature thermochronology, including fission-track and U-Th/He dating, has been widely used to constrain tectonic thermal evolution and ore deposits preservation. Understanding fission-track annealing and He diffusion kinetics in accessory minerals, such as zircon and apatite, is essential for dating and applications. In this study, previous zircon fission-track (ZFT) and apatite fission-track (AFT) ages in South China were collected. The result shows that the ZFT ages are mainly concentrated at 140–90 Ma, and the AFT ages are mainly distributed at 70–40 Ma. The age distribution and inversion temperature–time paths reveal heterogeneous exhumation histories in South China. The MLYB experienced Late Cretaceous-Cenozoic extremely slow exhumation after rapid cooling in the Early Cretaceous. The northern QHMB (i.e. from southern Anhui province to the Hangzhou Bay) had a relatively faster rate of uplifting and denudation than the southern QHMB in the Cretaceous. Subsequently, the northern QHMB rapidly exhumed, while the continuously slow exhumation operated the southern QHMB in the Cenozoic. The southern NLMB had a more rapid cooling rate than the northern NLMB during the Cretaceous time, and the whole NLMB experienced rapid cooling in the Cenozoic, except that the southern Hunan province had the most rapid cooling rate. The WYMB possibly had experienced slow exhumation since the Late Cretaceous. The exhumation thickness of the four metallogenic belts since 90 Ma is approximately calculated as follows: the MLYB $\leq$ 3.5 km, the northern QHMB concentrated at 3.5–5.5 km, and the southern QHMB usually less than 3.5 km, the NLMB 4.5–6.5 km and the WYMB $<$ 3.5 km. The exhumation thickness of the NLMB is corresponding to the occurrence of the world-class W deposits, which were emplaced into a deeper depth of 1.5–8 km. As such, we infer that the uplifting and denudation processes of the four metallogenic belts have also played an important role in dominated ore deposits.

Keywords Low-temperature thermochronology · Fission-track annealing and He diffusion kinetics · South China · Exhumation history · Deposits preservation

✉ Jian-Feng Gao
gaojianfeng@mail.gyig.ac.cn

[1] State Key Laboratory of Ore Deposit Geochemistry, Institute of Geochemistry, Chinese Academy of Sciences, Guiyang 550081, China

[2] University of Chinese Academy of Sciences, Beijing 100049, China

1 Introduction

Ore deposits preservation is known as an important part of the mineralization system (e.g., Wyborn et al. 1994; Zhai 1999; Kesler and Wilkinson 2006), mainly controlled by the emplacement depth of deposits and accumulated exhumation extent. The emplacement depth of ore deposits is associated with mineralization types. For example, the granite-related quartz-veins W deposits were emplaced at > 1.5–8 km. The porphyry deposits were usually emplaced at 1–6 km. The porphyrite Fe-apatite deposits were emplaced at < ~ 2 km and the magma-related hydrothermal deposits were usually emplaced at 0.05–1.5 km (Ye et al. 2014). Kesler and Wilkinson (2006) calculated the age-frequency distribution of porphyry Cu and epithermal and orogenic gold deposits and indicated that uplifting and denudation processes largely controlled the preservation of ore deposits. In detail, the ancient deposits might have been damaged by uplifting and denudation to some extent, with limited deposits preserved under specific tectonic settings, as exemplified by the Neoproterozoic porphyry Cu–Au mineralization in Jebel Ohier, preserved by temporal and spatial selection (Bierlein et al. 2016). While the too young deposits have not yet been discovered under the surface. As shown in Fig. 1, the shallower emplacement depth of ore deposits, the more significant effect of denudation (Kesler and Wilkinson 2006). The low-temperature hydrothermal deposits are relatively younger than the porphyry copper deposits, both of which mainly formed in the Neogene-Quaternary (Fig. 1). In contrast, the granite-related W(-Sn) deposits have much deeper emplacement depth, in which the most explored W(-Sn) deposits record Jurassic ages. Therefore, deposits preservation studies can provide insights into the ore explorations.

Low-temperature thermochronology includes $^{40}Ar–^{39}Ar$, fission-track, and U-Th(Sm)/He dating, which are sensitive to temperatures of ~ 40–350 °C and have different closure temperatures. A combination of various low-temperature thermochronology methods can provide detailed temperature–time information. Meanwhile, thermal inversion models based on fission-track annealing and He diffusion kinetics can reveal thermal histories. Therefore, it is efficient to reveal the uplifting and denudation history by applying low-temperature thermochronology, as exemplified by $^{40}Ar–^{39}Ar$ and apatite fission track studies on the Kesebir–Kardamos extensional dome, Bulgaria. The results revealed that the ~ 35 Ma sedimentary rock-hosted Au deposits emplaced during the early stage of basin formation, and experienced rapid cooling and exhumation at ~ 33–30 Ma (Márton et al. 2010). Liu et al (2014) conducted zircon and apatite U-Th/He studies of the Dexing porphyry Cu deposits and Yinshan porphyry-hydrothermal Ag–Pb–Zn–Cu deposits. The results indicated that the Dexing deposits had a more-exhumed extent than the Yinshan deposits.

South China is one of the most important metal resource provinces of China, where the distribution of different types of ore deposits is characteristic of the clusters and

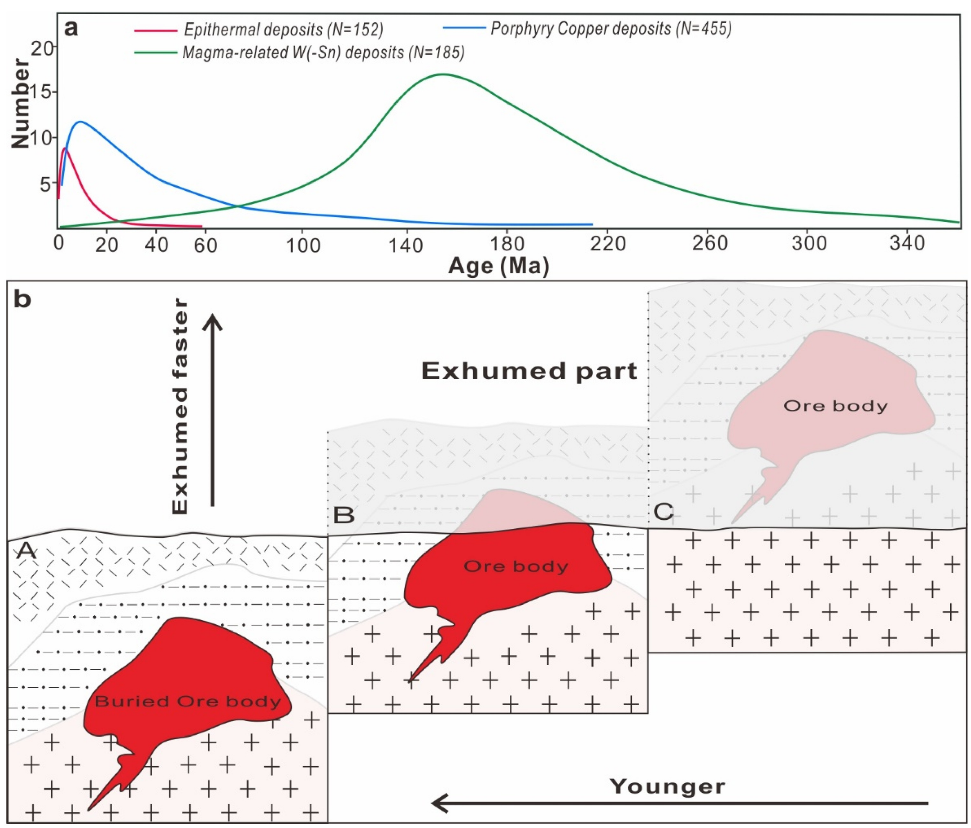

Fig. 1 **a**: Age-frequency distribution of epithermal deposits, porphyry copper deposits and granite-related W(-Sn) deposits. Age-frequency distribution of the porphyry copper deposits and low-temperature epithermal deposits are cited from Kesler and Wilkinson (2006). **b**: Simplified sketch map of the relationship between exhumation and ore deposits preservation

belts. There are four metallogenic belts: the Middle-Lower Yangtze River Metallogenic Belt (MLYB), Qinzhou-Hangzhou Metallogenic Belt (QHMB), Wuyi Metallogenic Belt (WYMB), and Nanling Metallogenic Belt (NLMB). The dominated deposit types in the MLYB are granite-related Cu–Au–Mo, porphyrite Fe-apatite. The QHMB is characterized by porphyry Cu (Au) and epithermal Pb–Zn–Ag deposits. The NLMB represents the most important W-Sn province, where intensive granite-related skarn-type and quartz-veins W-Sn deposits are distributed. The dominated mineralization in the WYMB is hydrothermal Cu–Au–Pb–Zn–Ag deposits. In this paper, we outline the method details of fission-track and U-Th(Sm)/He dating, with principles and patterns of application. The zircon and apatite fission tracks ages and inversion thermal models were used to infer the exhumation and preservation history of the ore deposits in South China. Furthermore, whether the distribution of ore deposits in the four metallogenic belts was affected by the uplifting and denudation processes was discussed.

2 Geological setting

The South China Block (SCB) (Fig. 2) is located in southeastern Asia, bounded by the north Qinling-Dabie Orogenic Belt, west Longmenshan Fault, and the Southwest Jinshajiang-Honghe Suture Zone. It experienced multiphase subduction, collision, and extension, after the amalgamation of the Yangtze Craton and the Cathaysia Block along the Jiangnan Orogenic Belt at ~ 830 Ma (e.g., Li and Zhao 2020). Briefly, the significant tectonic events of the SCB are as follows. The extensional setting and coeval magmatism and rift occurred at ~ 830–725 Ma (e.g., Yang et al. 2015; Duan et al. 2019). Intracontinental orogeny and subsequent tectonic extension operated at ~ 460–400 Ma (e.g., Li et al. 2010; Chen et al. 2020c). During Early Triassic to Late Jurassic, the SCB was collided and amalgamated with the North China Craton along the Qinling-Dabie Orogenic Belt (Li 2004) and amalgamated with the Indochina Block along the Jinshanjiang-Honghe Suture Zone at 250–200 Ma (Wan 2013b; Lepvrier et al. 2004). The Pacific Oceanic Plate had subducted beneath East Asia since the Early Jurassic, and the India Plate had been amalgamated with Eurasia by the Paleocene (e.g., Yin and Harrison 2000; Dong et al. 2008; Sun et al. 2021), which shaped the current SCB. Granitoids and volcanic rocks are widely distributed in the southeastern South China Block and formed at different periods: pre-Cambrian, Caledonian, Hercynian, Indosinian, and Yanshanian (Sun 2006). Especially, the Yanshanian granitoids and volcanic rocks occupy a total outcrop area of 203,790 km^2 (Zhou et al. 2006). Although Yanshanian I-, S- and A-type granites were reported in South China, the A-type

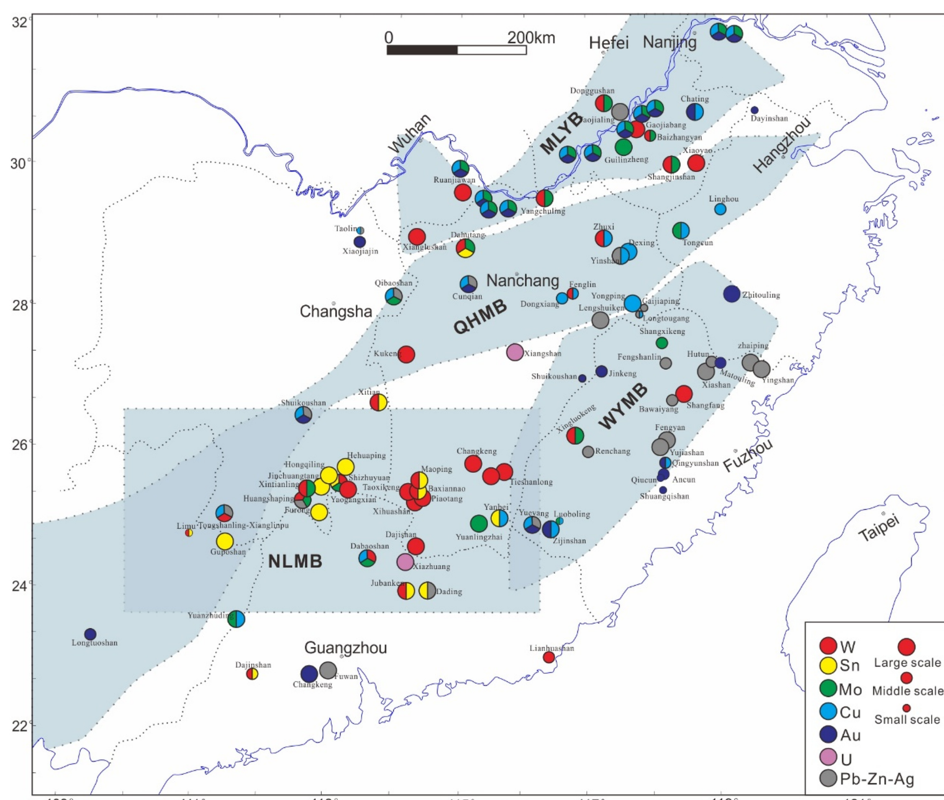

Fig. 2 Distribution of ore deposits in South China. QHMB: Qinzhou-Hangzhou Metallogenic Belt; MLYB: Middle-Lower Yangtze River Metallogenic Belt; WYMB: Wuyi Metallogenic Belt; NLMB: Nanling Metallogenic Belt

granites were mainly emplaced in the east-southeast coastline of South China in the late Yanshanian (e.g., Mao et al. 2013a; Chen et al. 2020b). The extensive and intense magmatism promoted the formation of various types of the Yanshanian ore deposits.

2.1 Spatial–temporal distribution of ore deposits in South China

South China is generally known as the world-class W-Sn mining province. In addition to the W-Sn deposits, magma-related Cu, Mo, Bi, Pb–Zn–Ag, Au, and REE ore deposits are widely distributed in South China (Fig. 2). Although the Mesozoic is the most important period of mineralization, there are some older and small-scale ore deposits in South China, such as the Silurian-Ordovician Qinjia skarn Sn-Cu, Niutangjie skarn W, and Liusha Mo deposits in the QHMB (Mao et al. 2013a), and the Indosinian granite-related Yuechengling-Miao'ershan W polymetallic deposits (Cheng et al. 2013). The dominated mineralization and representative deposits in four metallogenic belts are different.

In the MLYB, the dominated ore deposits are the Yanshanian magma-related Cu, Fe, S, Au, and Pb–Zn deposits. The mineralization was concentrated at $\sim$ 149–105 Ma (Zhou et al. 2015). For example, the Hehuashan MVT Pb–Zn deposit formed at 132.8 $\pm$ 3.1 Ma (Liu et al. 2021). The Chengmenshan and Xiangutai porphyry copper deposits formed at 144.8–149.3 Ma (Xu et al. 2021). The Chizhou porphyry Cu–Mo polymetallic deposit has molybdenite Re-Os ages of 151–148 Ma (Xie et al. 2019). The Paodaoling porphyry Au deposits, formed at $\sim$ 141–147 Ma (Duan et al. 2012). The Chating porphyry Cu–Au deposit records an average molybdenite Re-Os age of 136.0 $\pm$ 1.3 Ma (Xiao et al. 2020). The Magushan skarn Cu–Mo deposit formed at 134.2 $\pm$ 1.2 Ma (Li et al. 2020). The Anjishan and Tongshan Cu(Mo) deposits yield molybdenite Re-Os ages of 108 $\pm$ 2 Ma and 106 $\pm$ 3 Ma, respectively. Recently, with progressive exploration, some porphyry-skarn W(-Mo) deposits have been discovered in the MLYB, including the 146 Ma Yangchuling porphyry W–Mo deposit (Mao et al. 2017), the 146 Ma Gaojiabang skarn–porphyry W–Mo deposit, formed at 146.1 $\pm$ 4.8 Ma (Xiao et al.2017), the 142 Ma Ruanjiawan skarn W–Cu–Mo deposit (Deng et al.2015), the 146–135 Ma Baizhangyan skarn–porphyry W–Mo deposit(Li et al. 2015), the 140 Ma Shangjinshan skarn W–Mo deposit (Tang et al. 2019), the 126–123 Ma Xianglushan skarn W deposits (Dai et al. 2018), and the 97 Ma Donggushan skarn W-Mo polymetallic deposit (Nie et al. 2016).

The QHMB is an important intracontinental Mesozoic porphyry-skarn Cu-polymetallic metallogenic belt in South China (Yuan et al. 2018), extending from the northeastern Hangzhou Bay to the southwestern Qinzhou Bay (Fig. 2). The dominant resources in the QHMB are Cu, Mo, Au, Ag, and Pb–Zn. Representative deposits in the QHMB include the 161.8 $\pm$ 2.2 Ma Tongcun porphyry Mo(Cu) deposits (Li et al. 2013). In addition, the Qibaoshan porphyry-skarn Cu–Pb–Zn–Ag polymetallic deposit has a molybdenite Re-Os isochron age of 152.7 $\pm$ 1.7 Ma (Yuan et al. 2018). The Yuanzhuding porphyry Cu–Mo deposit records a molybdenite Re-Os isochron age of 155.6 $\pm$ 3.4 Ma (Xia et al. 2010). The Lengshuikeng porphyry Ag–Pb–Zn deposit formed at $\sim$ 162 Ma (Zuo et al. 2010). The Dexing porphyry Cu–Au–Mo deposit formed at $\sim$ 170 Ma (Liu et al. 2014), and adjacent Yinshan porphyry-hydrothermal Ag–Pb–Zn–Cu deposit formed at $\sim$ 176–166 Ma (Wang et al. 2012). In recent decades, serval W deposits have been explored in the QHMB, including the world-class Dahutang granite-related veinlets-disseminated W–Mo polymetallic deposit in the central QHMB, of which molybdenite yielded a Re-Os isochron age of 139.18 $\pm$ 0.97 Ma (Mao et al. 2013b). The large-scale Xiaoyao skarn W polymetallic deposit in the northern QHMB, of which molybdenite Re-Os dating yielded a weighted average age of 148.7 $\pm$ 2.3 Ma (Su et al. 2017). The world-class Zhuxi skarn W–Cu polymetallic deposit formed at $\sim$ 144–152.9 Ma (Liu et al. 2017). The Tongshanling-Xianglinpu skarn-hydrothermal W–Cu–Mo–Pb–Zn deposits formed at 162–158 Ma (Zhao et al. 2016). The Dayaoshan Caledonian granite-related W-Mo polymetallic deposit, located in eastern Guangxi, formed at $\sim$ 438–445 Ma (Chen et al. 2020c).

The WYMB is located in the southeast of the Cathaysia Block, including northern Guangdong, Fujian, and southern Zhejiang Provinces. The dominated resources in the WYMB are Cu–Au–Ag–Pb–Zn–Fe–W–Mo, associated with the Mesozoic volcanic-subvolcanic rocks, including the epithermal Ag–Pb–Zn, epithermal Cu–Au(Mo), epithermal Au, skarn Fe, and granite-related quartz-veins/veinlets-disseminated W-Mo deposits (Fig. 2). Some representative deposits are listed: the Yingshan epithermal Ag deposit with an ore-forming quartz inclusion Rb–Sr age of 107.6 $\pm$ 2.0 Ma (Lei 2020), the 112–102 Ma Zijinshan, Luoboling, and Yueyang epithermal Cu–Au–Mo–Ag ore fields (Zhang et al. 2003; Zhong et al. 2014; Zhao et al. 2020), the Makeng and Dayang Fe metallogenic deposits with molybdenite Re-Os ages and associated granite zircon U–Pb ages of 134–131 Ma (Zhang et al. 2012), the 162–158 Ma Qinyunshan epithermal Cu–Au deposit (Xiao et al. 2021), the 173 Ma Xiashan skarn Pb–Zn deposit (Xi et al. 2020), the 223 Ma Jinkeng epithermal Au polymetallic deposit (Wu 2021), the Shangfang skarn W deposit with a molybdenite Re-Os isochron age of 158.1 $\pm$ 5.4 Ma (Chen et al. 2013), and the 156–147 Ma

Xingluokeng quartz-veins/veinlets-disseminated W-Mo deposit (Zhang et al. 2008, 2020).

The NLMB is approximately located within ~ 110–116.5° E, ~ 23.5–26.5° N. Numerous Mesozoic granite batholites strike E-W and are distributed into three belts, with a ~ 110 km-interval (Zhou et al. 2006). The NLMB represents the largest W-Sn mineralization province, and the main mineralization occurred in the Middle Jurassic to Early Cretaceous, mainly at ~ 160–150 Ma (Mao et al. 2008). From the west to the east, the W mineralization changes from skarn to quartz-veins types, and the corresponding deposit resources decline, possibly resulting from the changing of the host rocks from carbonate to meta-clastic rocks (Mao et al. 2013a). Some typical deposits in the NLMB include the 128 Ma Yanbei porphyry Sn deposit (Li et al. 2007), the Tongshanling Pb–Zn polymetallic deposit with a garnet Sm–Nd isochron age of 173 ± 3 Ma (Wang et al. 2017), the 150 Ma Shizhuyuan skarn W–Sn–Wo polymetallic deposit ~ (Jiang et al. 2019), the 150 Ma Dajishan quartz-vein W polymetallic deposit (Zhang et al. 2006), the large-scale Huangshaping skarn W–Mo–Pb–Zn polymetallic deposit with a molybdenite Re-Os isochron age of 154.8 ± 1.9 Ma (Yao et al. 2007), the 162–157 Ma Xintianling skarn W–Mo deposit(Yuan et al. 2012), the Hehuaping skarn Sn polymetallic deposit experiencing three-phase mineralization at ~ 224, ~ 156–151, and 142 Ma (Cai et al. 2016), the Changkeng quartz-vein W deposit with a molybdenite Re-Os isochron age of 156.9 ± 2.0 Ma (Zhang et al. 2021), the 215–212 Ma Youmaling W deposits (Yang et al. 2015), and the 423–417 Ma Dushiling altered rock-skarn type W(Cu) deposit (Chen et al. 2016).

3 Analytic principles and methods

3.1 Fission track dating

The spontaneous nuclear fission (mainly ^{238}U) produces high-energy charged heavy particles (^{143}Ba and ^{90}Kr), which leave a trajectory of radioactive damage when passing through insulating or semiconducting solid materials (Fleischer et al. 1975). The details of the fission track dating theory can be seen in Donelick et al. (2005). It is similar to other radioactive isotope dating, the spontaneous tracks are counted as daughter isotope counterparts, described as the formula:

$$A_S = \frac{\lambda_f}{\lambda_D} \cdot {}^{238}\mathrm{U}\left(e^{\lambda_D t} - 1\right)$$

where A_S is the number of fission tracks today. Usually, the track number of a specific area of minerals is counted to represent A_S; λ_D is the ^{238}U decay constant; λ_f is the spontaneous fission constant of ^{238}U, $t_{1/2}$ was recommended as (8.2 ± 0.1) × 10^{15}a by IUPAC (Pure and Applied Chemistry, 2000, 72: 1525–1562). ^{238}U is the number of ^{238}U atoms; t is the time that fission track formed and preserved. These tracks could be visible under an optical microscope after chemical etching (Price and Walker, 1962). Price and Walker (1963) suggested and used spontaneous fission tracks as a radioactive dating method.

The fission track dating methods can be divided into two ways according to the measurement process of ^{238}U concentration. They are the external detector method and the population method, and the fission track dating by using LA-ICP-MS or EPMA. Both the external detector method and the population method determine ^{238}U by counting induced (^{235}U) fission tracks in low U-concentration mica or totally annealed samples (e.g., Nancy and Charles 1984). While the fission track dating based on LA-ICP-MS or EPMA straightly determines ^{238}U concentration or ^{238}U/^{43}Ca (^{30}Si or ^{91}Zr) (e.g., Hasebe et al. 2004; Dias et al. 2017; Vermeesch 2017). The method differences refer to Nancy and Charles (1984) and Gleadow (2002). The experiment procedures of fission track dating by LA-ICP-MS are as follow. (1) Sample mounting. Apatite grains are mounted in epoxy resins for polishing and etching, while zircons are usually settled in PFA Teflon because epoxy would be melted under an etching temperature of 225–230 °C. (2) Polishing and etching. The inner surface of grains is polished and etched to reveal the tracks. The AFT chemical etching protocol is etched 20 s at 21 °C in 5.5 M HNO_3, and the ZFT etching protocol is etched 4–120 h at 225–230 °C in eutectic 8.0 g KOH and 11.2 g NaOH (Gleadow et al. 1976). (3) Track data collection. The track density, D_{par} value, and latent track length are determined under an optical microscope. (4) Determination of ^{238}U concentration or ^{238}U/^{43}Ca for apatite and ^{238}U/^{30}Si (or ^{91}Zr) for zircon. (5) Age calculation and thermal history inversion.

The fission-track will be shortened or vanished (annealing) when the temperature is higher than that of partial annealing of the grains, as proved by fission track dating and experiments (e.g., Crowley et al. 1991; Liu et al. 2009). This annealing process is largely controlled by temperature, annealing period, grain component, crystal structure, and track geometry (the angle of track and crystallographic c-axis) (Fig. 3). Many annealing experiments were conducted to quantify the relationship among temperature, annealing time, and fission track age and length during the annealing process (e.g., Gleadow et al. 1986; Tagami et al. 1990; Crowley et al. 1991; Carlson et al. 1999). For apatite, the higher temperature and longer annealing time will result in more significant annealing. Also, chlorine and trace elements (REE, Mn, Fe, and Sr) contents or D_{par}

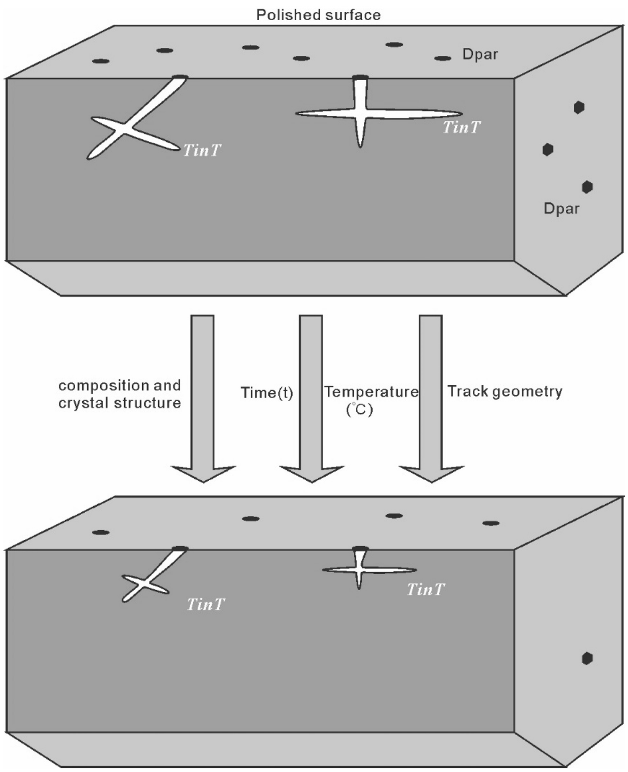

Fig. 3 Sketch map of apatite fission track annealing process. Fission track annealing is largely controlled by apatite component and structure, temperature, annealing time and angles between tracks and C-axis

values significantly control the annealing rate. Notably, radiation damage would greatly accelerate the fission-track annealing rate in the minerals, especially those with high U-concentration (e.g. zircon) and long-term damage accumulation (Kasuya and Naeser 1988; Hendriks and Redfield 2005). Therefore, quantification of zircon fission tracks annealing is complicated and challenging.

The apatite fission-track length distribution patterns are closely related to the annealing process (Fig. 4). It can be briefly divided into four patterns: (1) unimodal length cluster corresponding to rapid cooling; (2) unimodal length distribution corresponding to nearly constant speed cooling; (3) unimodal length distribution related to long time partial annealing with no reheating process; (4) bimodal length distribution indicating reheating during cooling with insufficient track annealing (Ketcham 2005). Therefore, the apatite fission-track length is usually used as an indicator of temperature changes in burying, and uplifting, and denudation processes. The inversion temperature–time models based on the fission-track length and Cl contents or D_{par} values (e.g., Crowley et al. 1991; Ketcham et al. 2007), conducted by software HeFTy or QTQt (Ketcham 2005; Gallagher 2012), are widely used to reveal the thermal history.

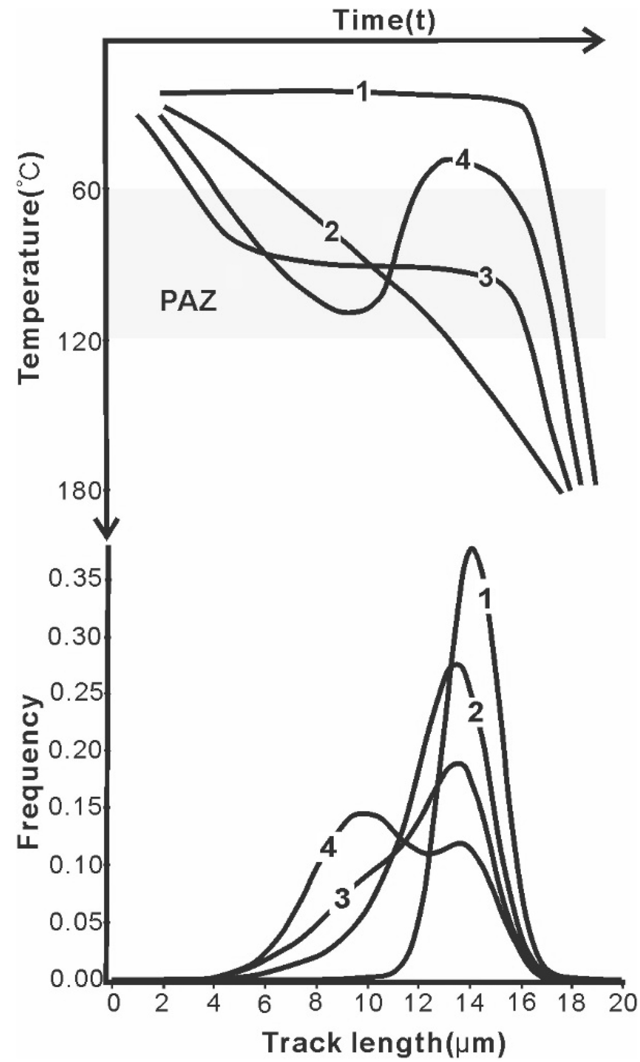

Fig. 4 Apatite cooling history and corresponding track length distribution pattern (according to Ketcham 2005, and conducted by HeFTy v2.0.0). PAZ: partial annealing zone. (1) rapid cooling; (2) cooling with nearly constant rate; (3) pass through partial annealing zone with low cooling rate without reheating process; and (4) reheating process during cooling without complete annealed

3.2 U-Th(Sm)/He dating

The U-Th(Sm)/He dating theory is similar to fission track dating. ^{4}He is formed and accumulated during the process of radioactive isotope decay. The main radionuclides include ^{147}Sm, ^{232}Th, ^{235}U, and ^{238}U, and the radioactive ^{4}He in minerals is expressed as the formula:

$$
\begin{aligned}
{}^4\mathrm{He} = {} & 8\,{}^{238}\mathrm{U}\left(e^{\lambda_{238}t}-1\right)+7\,{}^{235}\mathrm{U}\left(e^{\lambda_{235}t}-1\right) \\
& +6\,{}^{232}\mathrm{Th}\left(e^{\lambda_{232}t}-1\right)+{}^{147}\,\mathrm{Sm}\left(e^{\lambda_{147}t}-1\right)
\end{aligned}
$$

where ^{4}He is the total amount of radioactive ^{4}He; ^{147}Sm, ^{232}Th, ^{235}U, and ^{238}U is the number of ^{147}Sm, ^{232}Th, ^{235}U, and ^{238}U atoms, respectively. λ_{147}, λ_{232}, $\lambda_{235,}$ and λ_{238} is the decay constant of ^{147}Sm, ^{232}Th, ^{235}U, and ^{238}U. They are 6.54×10^{-12}/a, 4.9475×10^{-11}/a, 9.8485×10^{-10}/a, and 1.55125×10^{-10}/a, respectively; and t is the time. In addition, the half-time of ^{147}Sm ($t_{1/2} \approx 1.1 \times 10^{11}$ yr) is almost twenty-five times of ^{238}U, which means that in the geological history, ^4He produced by the radioactive decay of ^{147}Sm has a negligible effect on the U-Th/He dating results (e.g., Green et al. 2006). Hence, ^{147}Sm is usually not considered in the U-Th(Sm)/He dating measurement.

The initial ^4He produced by radioactive decay has high kinetic energies, which are largely controlled by mother radionuclides and range from ~ 4 eV to ~ 9 eV (Farley et al. 1996). ^4He is ejected to a random direction and the stopping distance depends on kinetic energy and density or composition of grains. As exemplified by ^{238}U and ^{232}Th decay in apatite and zircon, the radioactive ^4He would be ejected to ~ 10 to ~ 20 µm (Farley et al. 1996) and the distance in apatite is longer than that in zircon.

Additionally, from the inner to the surface of the grains, the probability of ^4He escape increases (Fig. 5). When the distance from the radionuclides in the grains to the grain surface is farther than the stopping distance, the decayed ^4He can only remain in the grains. However, as the distance decreases, the escape probability of ^4He gradually increases to 50%. It means that a sphere of 100 µm may only retain ~ 82% ^4He (Farley et al. 1996), and the ~ 82% ^4He residuals will yield a ~ 18% younger U-Th/He age. As such, the determination of the total ^4He amount is extremely important for dating. The total amount of ^4He is calculated based on the residual ^4He in the minerals and the correction factor F_T (Farley et al. 1996):

$$He_{total} = F_T \times He_{measure}$$

where He_{total} is the total amount of ^4He in the radionuclides decay process; $He_{measure}$ is the ^4He residual in the grains; F_T factor is controlled by the ^4He stopping distance and crystal surface to volume ratio. It assumes that there is no U and Th zonation in the grains, and the adjacent grains have little decayed ^4He (Fig. 5). The F_T value is calculated according to the grain density, radionuclide decayed alpha stopping distance and geometric parameters such as height and diameter of the grains. It has an assumption that the picked grains are specific geometry, such as ellipsoid, tetragonal prism, a tetragonal prism with one or two pyramids, hexagonal prism, etc. (Gautheron and Tassan-Got 2010; Ketcham et al. 2011). For U-Th/He dating of a single grain, the euhedral grains without inclusions and obvious cleavages were picked. However, in natural rocks, the separated minerals, like zircon and apatite, are usually fragmented, due to crystal growth defects or mechanical brokenness, which would indeed affect the accuracy of U-Th/He dating (Brown et al. 2013). For example, if the actual U-Th/He age of apatite is 74.5 Ma and the F_T value is measured as 0.722, the U-Th/He age will increase to ~ 75.2 Ma when 1% grain is missed, and to ~ 78.4 Ma when the lacked part increases to 5%. Although 3–5 grains of one sample were picked to determine the U-Th/He age, there can be noticeable dispersion. To avoid the picking and F_T value measurement errors, the alpha-ejection zone of the grains was polished before dating, which successfully solved the ^4He ejection influence. However, it may yield wrong ages if the grains are strongly zoned with uranium and thorium (e.g., Farley et al. 1996).

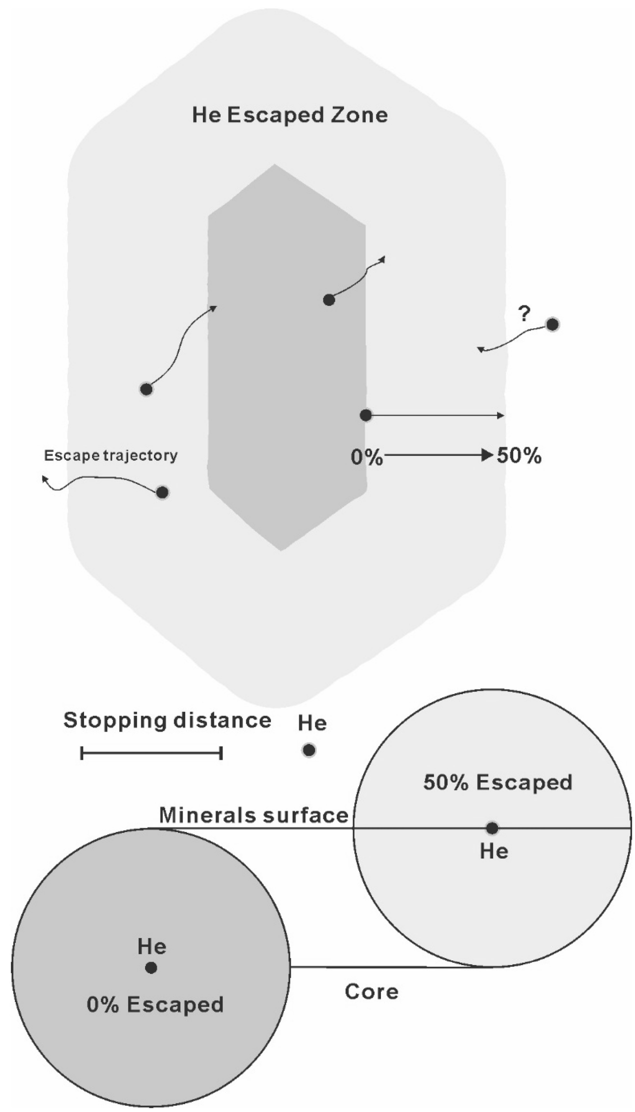

Fig. 5. ^4He ejection in grains. ^4He formed in the grain surface have 50% escaped from the grain, and the probability decreases to zero when the distance from the grain surface increases (stopping distance), shown as the 10% dark area; meanwhile, radionuclides in 30% dark area, the formed alpha particles can only remain in the grain

The brief procedure of U-Th/He dating is described as follows. (1) Grain picking and F_T value determination. The euhedral grains without abundant inclusions and visible cleavages were handpicked under a stereomicroscope. F_T

value calculation was conducted by software Qt Assistant 4.8.0 after the grain geometry was determined. (2) Grain package. Apatite and zircon grains are packaged in Pt and Nb tubes respectively to extract ^{4}He. (3) ^{4}He, ^{238}U, and ^{232}Th measurements. ^{4}He was extracted by a laser and measured by using the noble gas mass spectrometers. ^{238}U and ^{232}Th determination were conducted by an ICP-MS after the apatite or zircon grains were dissolved with isotope dilution techniques. In-site laser ablation apatite U-Th/He dating was successfully conducted by Pickering et al. (2020), the apatite grains were embedded into a Teflon FEP flam with a glass bead, whose diameter is known and used as an indicator to confirm the polishing depth of the grains (the ^{4}He stopping distance). The ^{4}He-ejection zones of apatite were polished. Then ^{4}He was extracted by a 33 μm laser beam, and mixed with a known volume ^{3}He. The ^{4}He/^{3}He ratio was measured by ASI Alphachron^{TM} quadrupole helium mass spectrometry system, and LA-ICP-MS was used to determine the U, Th, and Sm concentrations by a 55 μm laser beam covering the former pits. Both He-extraction and radionuclide concentration ablation pits were measured by optical profilometer to calculate ablation volume.

Similar to fission tracks annealing, the ^{4}He will be activated and escaped from the grains when the temperature is higher than its retention temperature, which is controlled by the diameter of crystals. Take an apatite grain with a 70 μm diameter and a 10 °C/Ma cooling rate, for example, the He closure temperature is ~ 70 °C, which will decrease to 62 °C for an apatite grain with a 60 μm diameter and 28 ppm *e*U (effective Uranium, $\approx U + 0.235 \cdot Th + 0.0046 \cdot Sm$, in zircon and apatite grains) (Farley 2000; RDAAM, Flowers, et al. 2009). The apatite and zircon partial retention zone (PRZ) are 50–80 °C and ~ 130–200 °C, respectively (e.g., Wolfe and Stockli 2010; Gautheron et al. 2013). Gautheron et al (2013) also proposed that the apatite composition influenced the He diffusion, similar to the apatite fission-track annealing, by changing the annealing rate of alpha-recoil damage. Furthermore, in some apatites, microvoids may trap helium, which affects the He diffusion kinetics and U-Th/He ages. The apatites with alpha-recoil damage have a higher He trapping power than the vacancy-clustering apatites (Gerin et al. 2017), implying that cleavages, vacancy damage, microvoids, and lattice defects in the minerals will significantly affect the He diffusion.

Radiation damage and temperature are widely accepted as the main controlling factors for the He diffusion (e.g., Nasdala et al. 2005; Ginster et al. 2019). The annealing of radiation damage is different from fission-track annealing, as it needs a higher temperature and longer time to completely reset the high radiation damage accumulation, and largely increases the He diffusion temperature. When the radiation damage exceeds the threshold of $\sim 3 \times 10^{16}$ α/g, the U-Th/He age will be abnormally older than the fission track age (e.g., Green et al. 2006; McDannell et al. 2019), indicating that the He diffusion efficiency is correlated with *e*U, time and temperature.

4 Principle of the application in ore deposits preservation

4.1 Sampling

Apatite and zircon are widely present in natural rocks, such as granite, diorite, tuff, sandstone, schist, gneiss, and mylonite. The hydrothermal alteration may change the composition of accessory minerals and produce a large number of secondary inclusions and fragile structures. Furthermore, hydrothermal or fault heat may cause a partial reset of the low-temperature thermochronology systems. Therefore, sampling was conducted far away from the hydrothermal or fault systems.

4.2 Various low-temperature thermochronology methods

The fission tracks partial annealing zone, He partial retention zone, and closure temperatures of apatite and zircon are different. The zircon fission track (ZFT) partial annealing temperature zone and closure temperature were estimated as ~ 200–350 °C and ~ 240 °C, respectively (Yamada et al. 1995; Tagami et al. 1996). The apatite fission track (AFT) partial annealing temperature zone and closure temperature were estimated as 60–120 °C and ~ 100 °C, respectively (Donelick et al. 2005) (Fig. 6). Various dating methods can provide the temperature–time information of thermal evolution by calculating cooling or uplifting and denudation rates of samples, as exemplified by n samples from the same location, the zircon fission-track age is Za_i and apatite fission-track age is Aa_i, the cooling rate could be described as:

$$\sum_{i=0}^{n} \{(T1_i - T2_i)/(Za_i - Aa_i)\}/n$$

where $T1$ and $T2$ are the closure temperatures of ZFT and AFT respectively; n is the number of samples. Similarly, apatite U-Th/He age ($A\mathrm{He}_i$) of samples, the cooling rate from AHe to present can be roughly determined as:

$$\sum_{i=0}^{n} \{(T3_i - T0)/A\mathrm{He}_i\}/n$$

where $T3_i$ is the apatite He closure temperature; $T0$ is the mean temperature of surface; n is the number of samples.

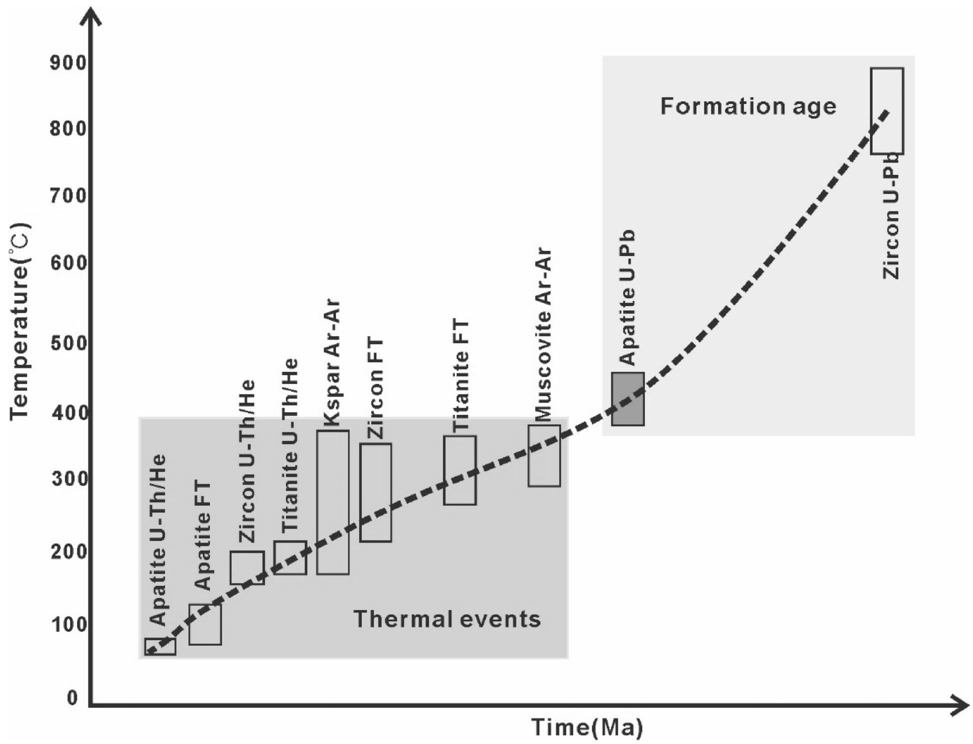

Fig. 6 Closure temperature of different dating systems

In addition, from the surface downwards, the low-temperature thermochronological ages of the samples gradually decrease to zero (Fig. 7A). For example, the apatite fission track ages of the Chinese Continental Scientific Drilling Project decreased from 87.1 ± 11.2 Ma at the surface to 3.2 ± 1.3 Ma at 3899 m depth (Liu et al. 2009). The zircon U-Th/He study of the Continental Deep Drilling Project (KTB) in Germany displays that the Zircon U-Th/He ages declined from ∼ 90 to 120 Ma at the surface to ∼ 0 Ma at ≥ 7790 m depth (Wolfe and Stockli 2010). The thermochronological age distribution [such as ZFT, zircon U-Th/He (ZHe), AFT and apatite U-Th/He (AHe) dating, etc.] can reveal the comparable cooling rate variations of samples. Figure 7B–E illustrate different zircon and apatite fission track age combinations, which reveal different cooling exhumation processes of continuous rapid uplifting

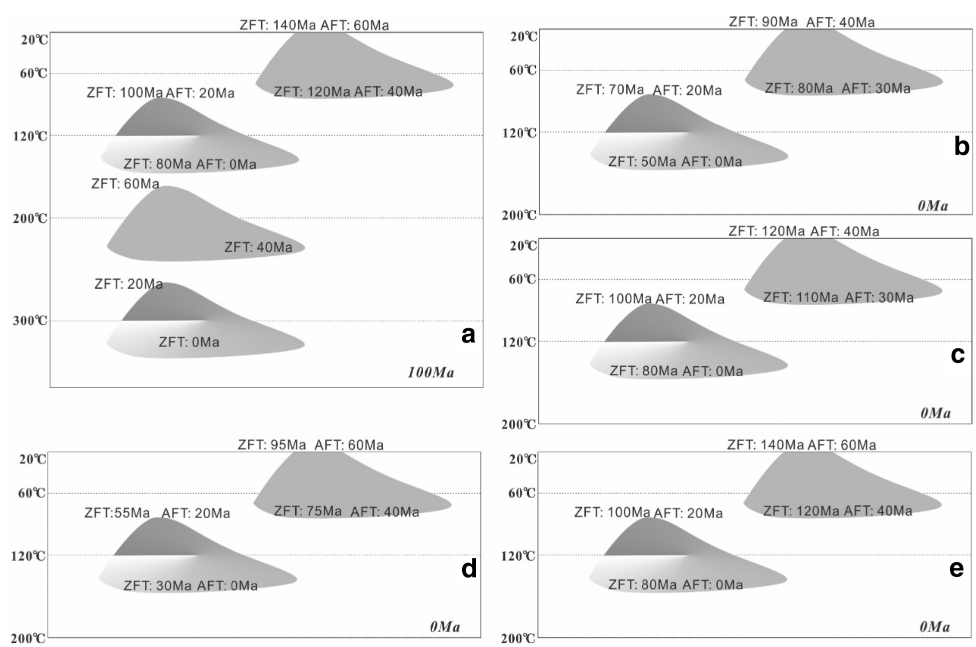

Fig. 7 Zircon and apatite fission track age distribution indicates rough exhumation histories. All age data were hypothesis, but based on the previous thermochronological studies. **A**: the zircon fission track and apatite fission track ages decrease from the surface to deep in 100 Ma; the present ZFT and AFT ages reflect the uplifting and denudation process. **B**: continuously rapid uplifting and denudation; **C**: slow exhumation and subsequent rapid uplifting and denudation; **D**: rapid exhumation and then turned into slow exhumation; and E continuous slow exhumation

and denudation (Fig. 7B), slow exhumation and subsequent rapid uplifting and denudation (Fig. 7C), rapid exhumation, and subsequent slow exhumation (Fig. 7D), and Slow exhumation (Fig. 7D).

4.3 Elevation-dating process

Thermochronological dating of samples at different elevations is another way to reveal the thermal history. The theoretical basis is that the shallower rocks first pass through the fission-track or the He closure temperature and the deeper rocks pass later, forming a fission-track or U-Th/He age gradient from the surface to the deep (Fig. 7A). Fission track or U-Th/He age of samples at different elevations can reveal the history of uplift and denudation in a certain period. The ages and elevation are used to calculate the cooling rate ($v_{(t1-t2)}$):

$$v_{(t1-t2)} = \frac{(H1 - H2) \cdot G}{t1 - t2}$$

where *H1* and *H2* are the samples elevations; *t1* and *t2* are the thermochronology ages; *G* is the geothermal gradient. Plotting elevation and ages of samples and the slopes of the curve are usually described as exhumation history.

5 Exhumation influence on deposit distribution in South China

5.1 Uplifting and denudation pattern in South China since the Late Cretaceous

Many low-temperature thermochronological studies were conducted to reveal the exhumation history of South China since the Mesozoic (e.g., Yi et al. 2009; Zuo 2015; Wang et al. 2020a; and reference here). These studies pointed out a similar exhumation history of South China, which generally includes three stages: Cretaceous rapid cooling, Late Cretaceous-Paleogene slow cooling process, and Oligocene-Quaternary rapid exhumation (e.g., Zuo 2015; Wang et al. 2015; and reference here). However, Zuo (2015) and Wang et al. (2020a) reported gradually older ages of ZFT and AFT from the interior to the southeastern coastline of South China and argued for a heterogeneous cooling history. To clarify the uplifting and denudation history of South China and the influence on ore deposits preservation, available ZFT and AFT ages and inversion thermal models were collected.

A total of 166 ZFT ages in previous studies of South China were compiled, in which most samples are granite, schist, gneiss, and tuff, with minor sedimentary rocks, and located within 21–30° N and 110–120.5° E (Peng et al. 2004; Li et al. 2005, 2007; Yi et al. 2009; Zheng et al. 2011; Wan 2013a, b; Guo 2004; Tang et al. 2014a; Wang et al. 2015, 2020a; Zuo 2015; Li 2017; Tao et al. 2017; Chen et al. 2020a). The data includes 129 ages passing the Chi-square Test (P(χ^2) > 5%), which indicates homogeneous, single thermal ages (Galbraith 1981). Another 37 ages failed the test, reflecting mixed thermal ages, which were not accepted in this study. It is noted that 10 ZFT ages were obtained for the Huangshan granite (Zheng et al. 2011), all of which failed the test. These single grain ZFT ages are negatively correlated with *e*U (or estimate alpha dose). Previous studies demonstrated that *e*U (or estimate alpha dose) will lower the thermal stability of fission-tracks in zircon (Kasuya and Naeser 1988) so that these ages might be affected due to low thermal stability. Although single grain ZFT ages range from 168 to 43 Ma, they have predominant distribution at 72–95 Ma, which is consistent with the continuous Cenozoic uplifting and denudation of southern Anhui province (ABGMR 1987). Therefore, the ages of 72–95 Ma are interpreted as the ZFT exhumation timing of the Huangshan granite, and an average ZFT age of 77 ± 8 Ma was used in this study.

The maximum ZFT age is 199 ± 16 Ma, and the minimum age is 60.4 ± 13.8 Ma (Supplementary data 1). Ages are mainly concentrated at 140–90 Ma, with peak ages at 120–90 Ma (Fig. 8). No obvious relationship between the ZFT age and elevation is illustrated (Fig. 9), indicating that complicated uplifting and denudation processes in South China at the Cretaceous. The ZFT age decrease with longitude increasing (108°–122°), but has no obvious relationship with latitude (Fig. 10). Ages decline regularly from the interior to the southeastern coastline (110°–122°), demonstrating the contrary tendency in Wang et al (2020a). In detail, from ~ 110° to 114° E, the ZFT ages decline rapidly, and from ~ 114° to ~ 122° E, the ages become slightly older (Figs. 10 and 14). It suggests that the Nanling region records the youngest ZFT ages in South China, which indicates the fastest cooling process of the Nanling region in the Cretaceous. From southeastern

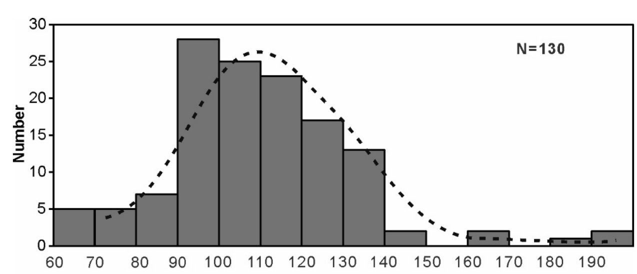

Fig. 8 ZFT age distribution pattern in South China. Data source from (Guo 2004; Peng et al. 2004; Li et al. 2005; Li 2017; Yi et al. 2009; Wang et al. 2015, 2020a; Wan 2013a; Tang et al. 2014a, b; Zuo 2015; Tao et al. 2017). 129 ZFT ages have passed the Chi-square Test (P(χ^2) > 5%), and the average ZFT age of 7

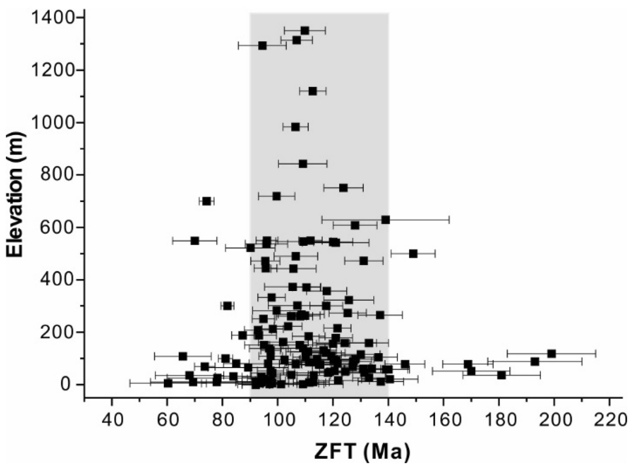

Fig. 9 Age-elevation plots of 129 ZFT data. There is no obvious relationship between ZFT ages and their elevations

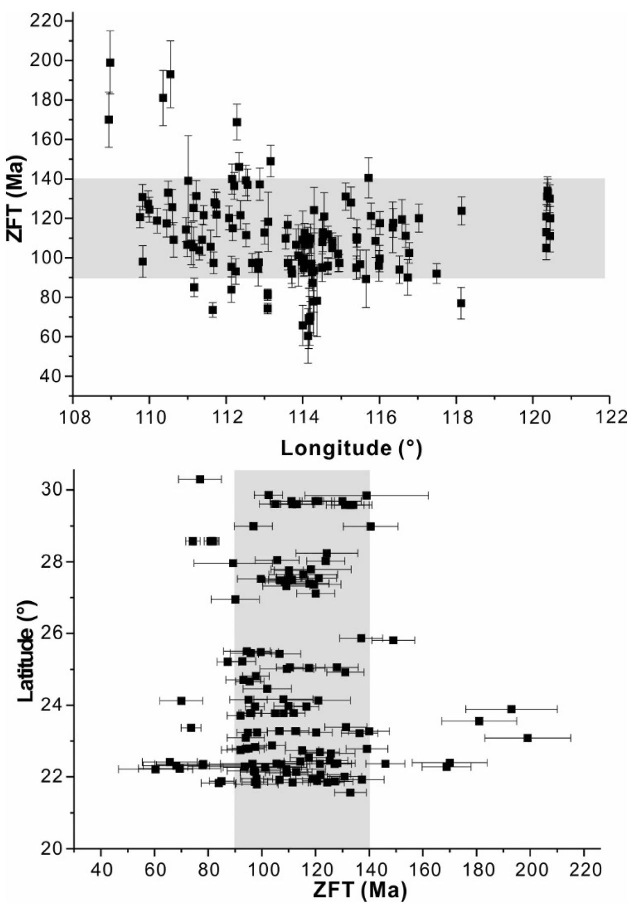

Fig. 10 Relationships between ZFT ages and longitudes and latitudes

South China to the interior, the cooling rate decreases in the Cretaceous, resulting in the older ZFT ages.

264 AFT ages were collected in this study (Peng et al. 2004; Li et al. 2005, 2016; Li 2017; Bai et al. 2006; Yi et al. 2009; Zheng et al. 2011; Shen et al. 2012; Shi et al. 2013; Wan 2013a; Guo 2004; Tang et al. 2014a, b; Wang et al. 2015, 2018, 2020a, b, 2021; Zuo 2015; Li 2017; Tao et al. 2017, 2019). Most samples are granite, schist, gneiss, mylonite, and tuff with some sedimentary rocks, diorite, and volcanic lava. 240 AFT ages have passed the Chi-square test [P(χ^2) > 5%], while 22 ages failed the test and 2 ages are larger than their formation age so that they were not chosen in this study. The maximum AFT age is 123.1 ± 7.6 Ma, whereas the minimum age is 11.3 ± 1.5 Ma. Ages are mainly distributed at 70–40 Ma, with a predominant cluster at 60–50 Ma (Supplementary data 1. Fig. 11). No obvious correlation between the AFT age and elevation was obtained (Fig. 12), indicating heterogeneous Cenozoic exhumation processes in South China. The AFT age is also not closely linked with longitude (Fig. 13). However, the AFT ages become older with latitude increasing (~ 20°–32° N), and the samples located in ~ 25°–27° N have youngest AFT ages of 40–10 Ma. Notably, the Tongling-Xuancheng area in the MLYB documents the oldest AFT ages, ranging from 66.9 ± 4.0 to 123.1 ± 7.6 Ma (Figs. 13 and 14). Zircon U-Th/He dating in this area were reported, which records simultaneous ages ranging from 88 to 140 Ma (Wang et al. 2021), indicating rapid cooling in the Cretaceous and slow exhumation in the Cenozoic.

To obtain detailed thermal evolution information of South China, we drew the ZFT and AFT age contours by using software Surfer® 17.1.288 (copyright © 1993–2019, Golden Software, LLC). The central ages of ZFT and AFT have been used in this study. All ZFT/AFT ages with their locations were calculated to grid data by the Kriging-Variogram method. The obtained contour map is shown in Fig. 14. There is no obvious tendency between the ZFT and AFT ages in South China. Notably, the four belts have different ZFT and AFT age distributions, indicating different cooling histories. The inversion temperature–time models were selected to understand the cooling histories (Fig. 15). The ZFT and AFT age distributions of the four metallogenic belts and their possible exhumation process are detailed as follows.

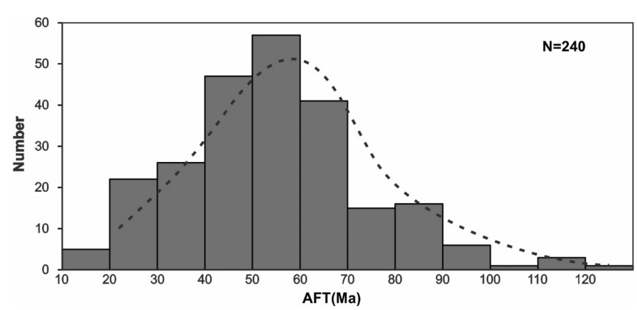

Fig. 11 AFT age distribution pattern in South China. Data source from (Guo 2004; Peng et al. 2004; Li et al. 2005; Li 2017; Yi et al. 2009; Wang et al. 2015, 2020a, b; Wan 2013a; Tang et al. 2014a, b; Zuo 2015; Tao et al. 2017)

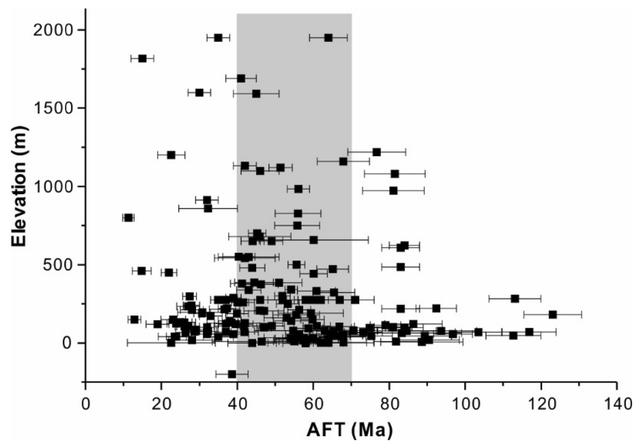

Fig. 12 Age-elevation plots of 182 AFT age data. There is no obvious relationship between AFT ages and their elevations

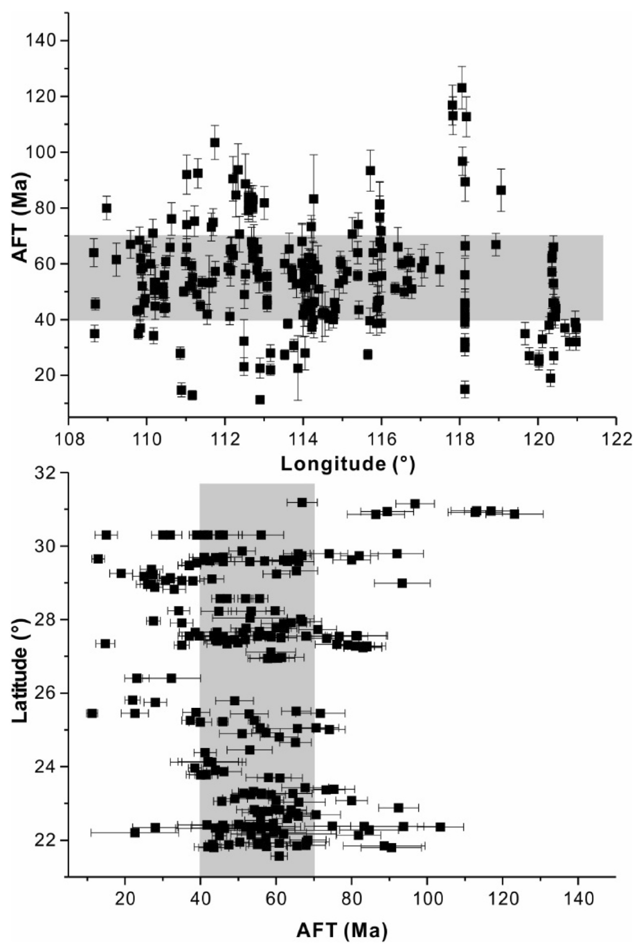

Fig. 13 Relationships between 240 AFT ages and longitudes and latitudes

5.1.1 The MLYB exhumation pattern since the Cretaceous

Although the corresponding ZFT ages are lacking, the zircon U-Th/He ages of 140–88 Ma revealed rapid cooling in the Cretaceous. The Mesozoic igneous rocks in the MLYB formed at 153–120 Ma. Furthermore, the younger A-type granite (135–120 Ma) is distributed in the central MLYM, indicating an extensional setting at the Early Cretaceous (Chen et al. 2020b). In addition, the MLYB records the oldest AFT ages (123–77 Ma) in South China (mostly at 70–40 Ma). Thus, the ZHe and AFT age distributions imply that the MLYB has experienced slow uplifting and denudation after the rapid cooling in the Early Cretaceous (Fig. 15A), inducing exposure of the Mesozoic igneous rocks and magma-related deposits on the surface.

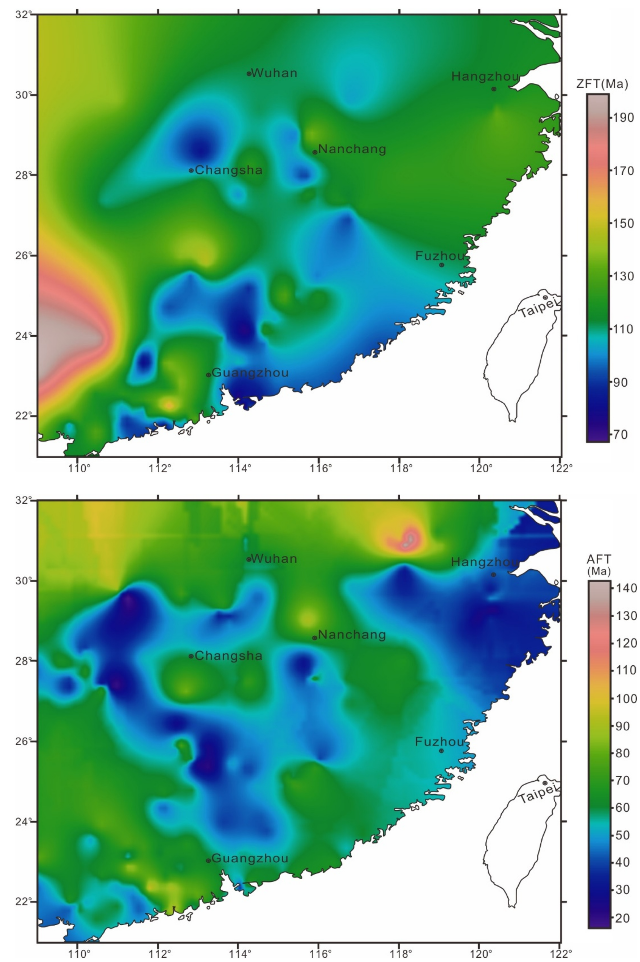

Fig. 14 Contour map of ZFT and AFT ages in South China

5.1.2 The QHMB exhumation pattern since the Cretaceous

The QHMB has the oldest ZFT ages in South China, especially the Shiwandashan region in the southern QHMB has the ZFT ages of 199–170 Ma (Guo 2004), implying a slow exhumation process in the Cretaceous, whereas the northern QHMB has a relatively faster rate of uplifting and denudation than the southern part. The southern QHMB has older AFT ages than the northern QHMB. The AFT age distributions in the QHMB are similar to the ZFT ages.

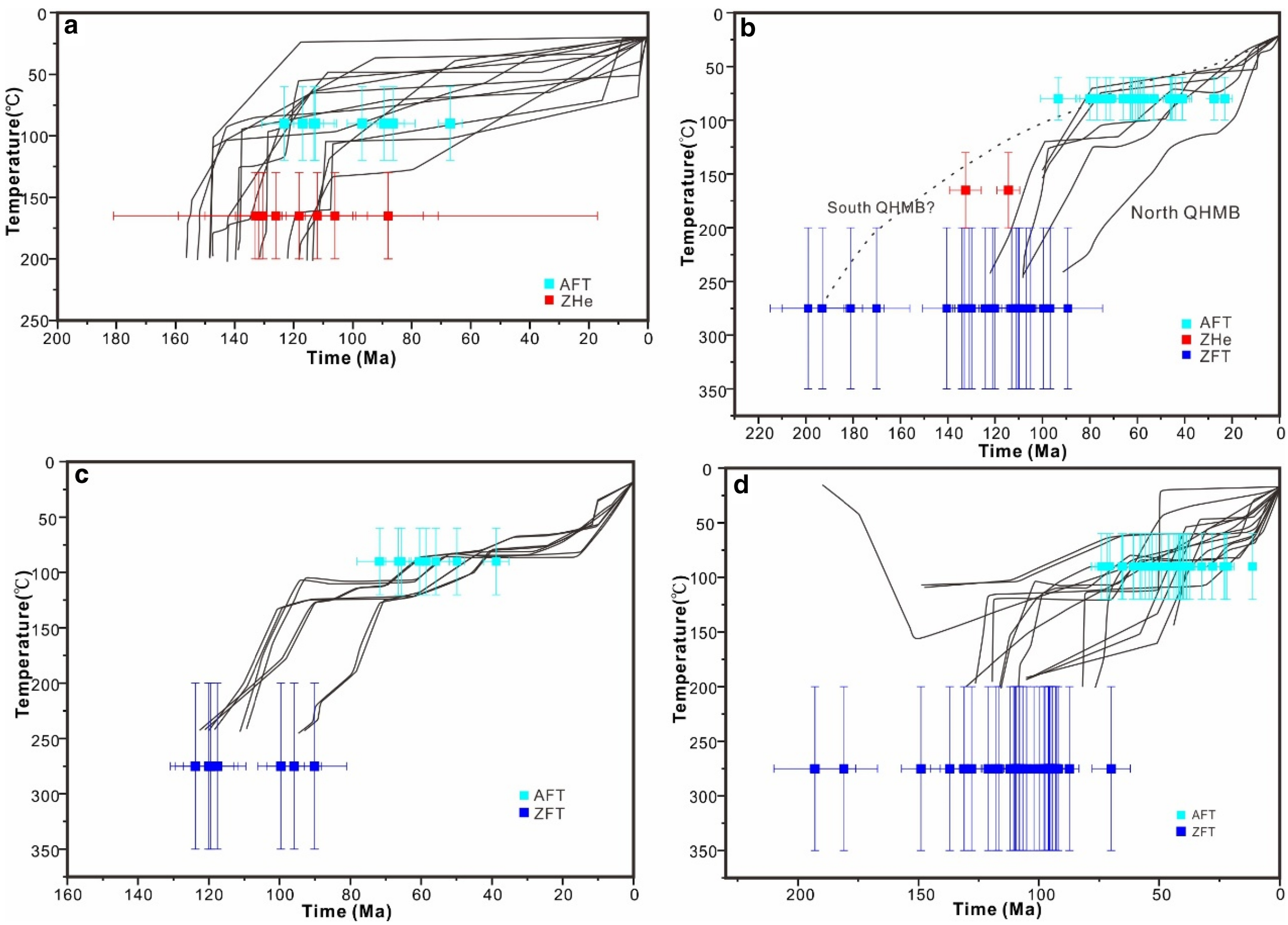

Fig. 15 The inversion temperature–time paths of four metallogenic belts. **A**: Middle-Lower Yangtze River Metallogenic Belt; **B**: Qinzhou-Hangzhou Metallogenic Belt; **C**: Wuyi Metallogenic Belt; D: Nanling Metallogenic Belt. The dark lines are the best paths of inversion models. ZFT, ZHe and AFT are thermochronology data of the four metallogenic belts. The paths and data are cited from Guo (2004), Yi et al (2009), Liu et al (2014), Zuo (2015), Li (2017), Tao et al (2017, 2019), Wang et al (2020a, 2021), and Min et al (2020)

From the Hangzhou Bay to the southern Anhui Province, the AFT ages are distributed at ~ 30–20 Ma, younger than the peak ages of 70–40 Ma in South China. Meanwhile, the AFT ages in the central and southern QHMB are mainly distributed at 80–50 Ma. The ZFT and AFT age distributions indicate that the southern and central QHMB had experienced continuously slow exhumation since the Cretaceous, whereas the northern QHMB was slowly uplifted and eroded during the Cretaceous time and rapid uplifting and denudation during Cenozoic time (Fig. 15B).

5.1.3 The WYMB exhumation pattern since the Cretaceous

There are only a few thermochronological studies in the WYMB (e.g., Li 2017; Wang et al. 2020a). The WYMB has much older ZFT and AFT ages compared to the other belts in South China, according to the available thermochronologic data (e.g., sample 01GF-222 from Wang et al. 2020a, located at 27.119° N, 117.025° E with the ZFT and AFT ages of 120.1 ± 7.1 Ma and 58.6 ± 6.6 Ma, respectively; sample 01JF-214 located at 28.015° N, 118.139° E, with the ZFT and AFT ages of 123.8 ± 7.1 Ma and 66.5 ± 3.6 Ma, respectively, etc.). The WYMB might have undergone continuously slow uplifting and denudation since the Late Cretaceous (Fig. 14). The inversion temperature–time paths indicate that the WYMB experienced rapid cooling in the Early Cretaceous and continuous slow exhumation since the Late Cretaceous (Fig. 15C).

5.1.4 The NLMB exhumation pattern since the Cretaceous

The NLMB has a uniquely uplifting and denudation history. The ZFT age distribution is different from the southern to northern NLMB. The southern NLMB has the youngest ZFT ages of 110–70 Ma in South China (Figs. 10 and 14), whereas the ZFT ages are mainly distributed at 140–110 Ma in the northern NLMB, indicating that the southern NLMB underwent more rapid cooling than the northern NLMB in the Cretaceous. The AFT ages in the NLMB range from 11.3 ± 1.5 to 74.1 ± 4.2 Ma, with most clusters at 60–40 Ma. The AFT age distribution in the NLMB is nearly uniform, but the northwest NLMB (i.e. the southern Hunan Province) is different and has the youngest AFT ages of ~ 40–10 Ma (Figs. 13 and 14). The ZFT and AFT age distributions imply that the cooling rate increases from north to south-southeast in the NLMB during the Cretaceous. In the Cenozoic, the whole NLMB was uplifted and denuded rapidly, but the northwestern NLMB demonstrated the exhumation most rapid rate (Fig. 15D).

5.2 Denudation influence on deposit distribution in South China

The uplifting and denudation processes resulted in a different exhumation in the four metallogenic belts. The continuously rapid exhumation makes the NLMB experiencing the most significant exhumation, whereas the WYMB and MLYB may have only undergone limited exhumation since the late Cretaceous.

In this study, the zircon and apatite fission tracks are assumed to have a constant closure temperature of 240 and 100 °C, respectively, and the geothermal gradient in South China is constant. The present geothermal gradients in South China range from 7.8 to 162.5 °C/km, mostly concentrated at 20–25 °C/km with an average value of 24.1 °C/km (Yuan et al. 2006). However, affected by the Cenozoic magmatism (e.g., Ho et al. 2003), the east coastline of Fujian Province has an extremely high geothermal gradient of ~ 73–85 °C/km. The geothermal gradient is largely associated with tectonic and thermal events (Wang et al. 2001), implying that South China has had a higher mean geothermal gradient since the late Cretaceous. Thus, we used 35 °C/km as the geothermal gradient of South China since the Cretaceous and calculated the exhumation amount since 90 Ma. The results are shown that the MLYB exhumed $\leq$ 3.5 km since 90 Maand the northern and southern QHMB experienced different uplifting and denudation processes, with an exhumed thickness of 3.5–5.5 km and $\leq$ 3.5 km respectively (Fig. 16). The WYMB exhumed about 3.5–5.5 km according to the contour map (Fig. 16), but its exhumed thickness calculated from the available data is ~ 3.5 km. The WYMB may have experienced slow exhumation since the Late Cretaceous, and we considered an exhumation amount of < ~ 3.5 km. The NLMB exhumed about 4.5–6.5 km, agreeing well with its continuous rapid uplifting and denudation processes since the Cretaceous.

The porphyrite Fe-apatite and porphyry Cu–Mo–Au deposits are the dominant mineralization in the MLYB. The emplacement depth of these Cretaceous ore deposits is generally 1–6 km, and the porphyrite Fe-apatite deposits are emplaced at < 2 km. The 1.5–3.5 km exhumation amounts are reasonable to induce shallow deposits exposed to the surface or close to the surface. Liu et al (2012) conducted the AFT studies on four porphyrite Fe deposits in the Luzong and Ningwu basins. The AFT ages and thermal inversion models indicate that these Fe deposits experienced slow uplifting and denudation and exhumed less than 2 km. Furthermore, the Dongshan and Meishan Fe deposits were exposed to the surface due to the faster exhumation rate, whereas the Luohe and Nihe Fe deposits are still buried. Similar uplifting and denudation processes are revealed in the adjacent Fengshandong porphyry Cu–(Mo) and Jilongshan skarn Au–Au deposits (Li Yan, unpublished data). The northern and southern QHMB has experienced different uplifting and denudation processes. The southern QHMB exhumed < 3.5 km since 90 Ma, while the northern QHMB possibly exhumed ~ 3.5–5.5 km. The AFT, AHe, and ZHe studies on the Dexing porphyry Cu and Yinshan epithermal Ag–Pb–Zn–Cu deposits indicate similar exhumation histories of these two ore deposits, but the Dexing had more uplifted and denuded amounts of ~ 1 km than the Yinshan since the Late Cretaceous (Liu et al. 2014; Min et al. 2020). The NLMB had exhumed 4.5–6.5 km since the Late Cretaceous, resulting in the deep-emplaced granite-related W(Sn) deposits exposed to the surface. As exemplified by the Qianlishan granite (Wan 2013a), the ZFT and AFT ages indicated the Cretaceous slow exhumation and Cenozoic rapid uplifting and denudation processes. The granitic pluton and related W deposits (such as Shizhuyuan, Hongqiling, Yaogangxian, etc.) were uplifted and denudated to the surface. The available ZFT and AFT data indicates the continuously slow exhumation for the WYMB, which was possibly uplifted and denuded < ~ 3.5 km since 90 Ma. Notably, the preservation of abundant epithermal ore deposits in the WYMB suggests that the exhumed amounts may be < 1.5 km since the deposits were formed at ~ 223–100 Ma (Fig. 15C). Thus, the WYMB might have experienced slow uplifting and denudation since the Late Cretaceous.

The dominant ore deposit types in the four metallogenic belts were probably affected by the amounts of exhumation due to different formation depths of ore deposits. The NLMB has the most exhumation amounts with the major mineralization of deeply-formed granite-related W-Sn. In contrast, the W deposits explored in the MLYB, QHMB, and WYMB in decades suggest that these metallogenic belts might have great potential for W mineralization, but the amounts of exhumation are not enough to make these deposits exposed to the surface.

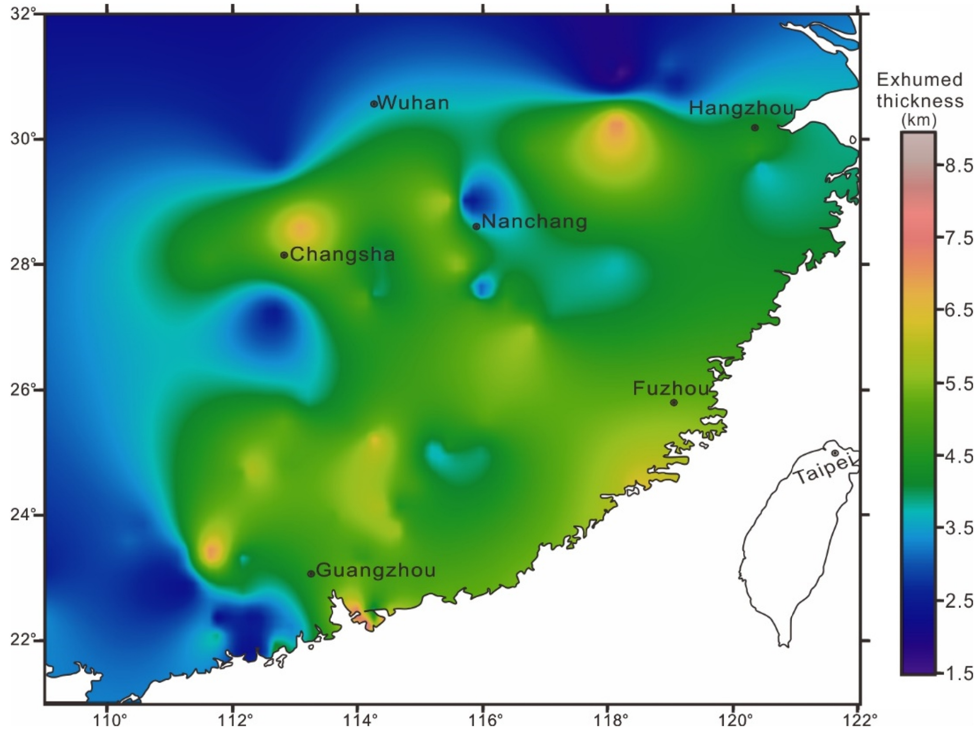

Fig. 16 The accumulated exhumation thickness distribution of South China since 90 Ma, calculated according to the ZFT and AFT ages. Geothermal gradient is assumed as 35 °C/km and the average surface temperature is 20 °C

6 Conclusions and problems

Low-temperature thermochronology, such as fission-track and U-Th/He dating, is sensitive to temperature and has different closure temperatures. Furthermore, the spontaneous fission-track annealing and radioactive ^{4}He diffusion in the minerals are associated with temperature and time, which are usually used in the studies of thermal history and ore deposits preservation. Based on previous ZFT and AFT data, the qualitative exhumation framework of South China was established:

Different uplifting and denudation processes were operated in South China. The MLYB experienced rapid cooling in the Early Cretaceous, followed by very slow exhumation in the Late Cretaceous-Cenozoic, with the denudation amounts less than 3.5 km. The northern QHMB had a faster rate of uplifting and denudation than the southern QHMB in the Cretaceous. Similarly, the northern QHMB (i.e. the southern Anhui Province to the Hangzhou Bay) was rapidly exhumed in the Cenozoic, while the southern QHMB kept slow exhumation. The available exhumed thickness of the northern and southern QHMB is 3.5–5.5 km and $\leq$ 3.5 km, respectively. The WYMB had possibly experienced continuously slow uplifting and denudation since the Late Cretaceous, and more low-temperature thermochronological studies are needed to constrain its thermal evolution process. Based on the available data and geological evidence, the exhumation amounts of WYMB since the Late Cretaceous may be less than ∼ 3.5 km. The southern NLMB has a much more rapid cooling rate than the northern NLMB in the Cretaceous, and the whole belt underwent rapid cooling in the Cenozoic. The calculated amount of the exhumation since 90 Ma for the NLMB is 4.5–6.5 km. Correspondingly, the dominant ore deposits in the NLMB are granite-related W-Sn deposits, the emplacement depths of which are generally 1.5–8 km, whereas the other three metallogenic belts are predominantly ore deposits with shallow emplacement depths. Therefore, the uplifting and denudation processes of South China have played an important role in controlling the types and distribution of dominated ore deposits in the four metallogenic belts.

Although the fission-track and U-Th/He dating have been successfully used to reveal the thermal evolution and ore deposits preservation, both methods have some unresolved problems. Minerals component, structure, radioactive damage, temperature, and time are proved to control the fission-track annealing and He diffusion. The fission-track length is used as an indicator of track annealing. However, the chemical etching protocols (apatite fission track: 20 s, 21 °C, 5.5 M HNO_3; zircon fission track: 4–120 h, 225–230 °C in eutectic KOH and NaOH) are usually failed to reveal full latent tracks (Tamer and Ketcham 2020), indicating that the fission-track annealing models may be challenging. The radioactive damage also largely affects tracks annealing and He diffusion (e.g., Green et al. 2006; McDannell et al. 2019). The high-radiation damage will significantly reduce the track annealing temperature but increase the He diffusion temperature (e.g., McDannell et al. 2019; Ginster et al. 2019). Quantifying the effects of composition, structure, and radiation damage on track annealing and He diffusion temperatures is difficult and challenging. Furthermore, the He diffusion models of zircon (ZRDAAM, Gautheron et al. 2013) and apatite (RDAAM, Flowers et al. 2009) assume the effective spontaneous fission tracks as a proxy of accumulated radiation damage. However, He diffusion is not consistent with track annealing, questioning the established models. The estimation of U-Th/He and fission-track closure temperatures in the grains associated with component, structure, and α-damage is key to defining the thermal evolution process.

Supplementary Information The online version contains supplementary material available at https://doi.org/10.1007/s11631-021-00506-x.

Acknowledgements This manuscript is supported by the National Science Fund for Distinguished Young Scholars (42025301) and Natural Science Foundation of China (41673057). We are grateful to Dr. Liu Qian of the University of Hong Kong for several constructive comments and polishing our language.

Author contributions All authors contributed to the conception and design study. Data collection and analysis: MK; Writing, original draft preparation: MK; Writing, review and editing: JFG. All authors read and approved the final manuscript.

Declarations

Conflict of interest We declare no conflicts of interest in this study. The manuscript has not been submitted to more than one journal for simultaneous consideration.

References

ABGMR (Anhui Bureau of Geology and Mineral Resources) (1987) ABGMR (Anhui Bureau of Geology and Mineral Resources) regional geology of the Anhui Province. Geological Press, Beijing, pp 165–191 (**in Chinese with English summary**)

Bai DY, Huang JZ, Meng DB, Ma TQ, Wang XH, Zhang XY, Chen BH (2006) Meso-cenozoic thermochronological analysis of the uplift process of mountains in Southeast Hunan. Acta Geosci Sin 27(6):525–536 (**in Chinese with English abstract**)

Bierlein FP, Reynolds N, Arne D, Bargmann C, Mckeag S, Bullen W, Al-Athbah H, McKnight S, Maas R (2016) Petrogenesis of a neoproterozoic magmatic arc hosting porphyry Cu-Au mineralization at Jebel Ohier in the Gebeit Terrane, NE Sudan. Ore Geol Rev 79:133–154

Brown RW, Beucher R, Roper S, Persano C, Stuart F, Fitzgerald P (2013) Natural age dispersion arising from the analysis of broken crystals. Part i: theoretical basis and implications for the apatite (U-Th)/He thermochronometer. Geochim Cosmochim Acta 122(3):478–497

Cai MH, Zhang WB, Peng ZA, Liu H, Guo TF, Tan ZM, Tang LF (2016) Study on minerogenetic epoch of the Hehuaping tin-polymetallic deposit in southern Hunan. Acta Petrol Sin 32(07):2111–2123 (**in Chinese with English abstract**)

Carlson WD, Donelick RA, Ketcham RA (1999) Variability of apatite fission-track annealing kinetics: I. Exp Results Am Miner 84(9):1213–1223

Chen CH, Lee CY, Tien JL, Xiang H, Walia M, Lin JW (2020a) Post-orogenic thermal reset of the Pingtan-Dongshan metamorphic belt (SE China): insights from zircon fission track and U-Pb double dating. J Asian Earth Sci 201(3):104512

Chen L, Zheng YF, Zhao ZF (2020b) Origin of arc-like magmatism at fossil convergent plate boundaries: Geochemical insights from Mesozoic igneous rocks in the middle to lower Yangtze Valley, South China. Earth Sci Rev 211:103416

Chen MH, Dang Y, Zhang ZQ, Chen G, Huang ZZ, Ye YL (2020c) Caledonian tungsten deposits in Dayaoshan area of South China. Miner Depos 39(4):647–685 (**in Chinese with English abstract**)

Chen RS, Li JW, Cao K, Qu CY, Li YJ (2013) Zircon U-Pb and molybdenite re-os dating of the Shangfang Tungsten deposit in Northern Fujian Province: implications for regional mineralization. Earth Sci J China Univ Geosci 38(02):289–304 (**in Chinese with English abstract**)

Chen WD, Zhang WL, Wang RC, Chu XY, Xiao R, Zhang D, Che XD (2016) A study on the Dushiling tungsten-copper deposit in the Miao'ershan-Yuechengling area, Northern Guangxi, China: implications for variations in the mineralization of multi-aged composite granite plutons. Scientia Sinica Terrae 46(12):1602–1625

Cheng SB, Fu JM, Ma LY, Jiang GX, Chen XQ, Lu YY, Tong XR (2013) Indosinian metallogenic activity in Yuechengling-Miaoershan area, northeastern Guangxi: implications from zircon U-Pb ages and Hf isotopic constraint on ore-forming granites in Youmaling and Jiepai deposits. Geol China 40(04):1189–1201 (**in Chinese with English abstract**)

Crowley KD, Cameron M, Schaefer RL (1991) Experimental studies of annealing of etched fission tracks in fluorapatite. Geochim Cosmochim Acta 55:1449–1465

Dai P, Mao JW, Wu SH, Xie GQ, Luo XH (2018) Multiple dating and tectonic setting of the Early Cretaceous Xianglushan W deposit, Jiangxi Province, South China. Ore Geol Rev 95:1161–1178

Deng XD, Li JW, Zhou TF, Zhao XF, Dai RY (2015) In-situ LA-ICPMS trace elements and U-Pb analysis of titanite from the Mesozoic Ruanjiawan W–Cu–Mo skarn deposit, Daye district, China. Ore Geol Rev 65(43):990–1004

Dias ANC, Chemale JF, Soares CJ, Soares CJ (2017) A new approach for electron microprobe zircon fission track thermochronology. Chem Geol 459:129–136

Donelick RA, O'Sullivan PB, Ketcham RA (2005) Apatite fission-track analysis. Rev Miner Geochem 58:49–94

Dong SW, Zhang YQ, Long CX, Yang ZY, Ji Q, Wang T, Hu JM, Chen XH (2008) Jurassic tectonic revolution in China and new interpretation of the "Yanshan Movement." Acta Geol Sin Engl Ed 82(2):334–347

Duan LA, Yang XY, Wang FY, Deng JH, Sun WD (2012) Geochemistry and zircon U-Pb age of ore-bearing porphyry in the Paodaoling gold deposit in Guichi, Middle-Lower Yangtze metallogenic belt. Acta Petrol Sin 28(10):3241–3254 (**in Chinese with English abstract**)

Duan Z, Liao SB, Chu PL, Huang WC, Zhu YH, Shu XJ, Li CB (2019) Zircon U-Pb ages of the Neoproterozoic Jiuling complex granitoid in the eastern segment of the Jiangnan orogeny and its tectonic significance. Geol China 38(06):1143–1153 (**in Chinese with English abstract**)

Farley KA (2000) Helium diffusion from apatite: general behavior as illustrated by Durango fluorapatite. J Geophs Res 105:2903–2914

Farley KA, Wolf RA, Silver LT (1996) The effects of long alpha-stopping distances on (U-Th)/He ages. Geochim Cosmochim Acta 60(21):4223–4229

Fleischer RL, Price PB, Walker RL (1975) Nuclear tracks in solids. University of California Press, Berkeley, pp 1–629

Flowers RM, Ketcham RA, Shuster DL, Farley KA (2009) Apatite (U–Th)He thermochronometry using a radiation damage accumulation and annealing model. Geochim Cosmochim Acta 73(8):2347–2365

Galbraith RF (1981) On statistical estimation in fission track dating. J Int Assoc Math Geol 16(7):653–669

Gallagher K (2012) Transdimensional inverse thermal history modeling for quantitative thermochronology. J Geophys Res Solid Earth 117(B2):53493394

Gautheron C, Barbarand J, Ketcham RA, Tassan-Got L, Peter VDB, Pagel M, Pinna-Jamme R, Couffignal F, Fialin M (2013) Chemical influence on α-recoil damage annealing in apatite: implications for (U-Th)/He dating. Chem Geol 351:257–267

Gautheron C, Tassan-Got L (2010) A monte carlo approach to diffusion applied to noble gas/helium thermochronology. Chem Geol 273(3–4):212–224

Gerin C, Gautheron C, Oliviero E, Bachelet C, Djimbi DM, Seydoux-Guillaume AM, Tassan-Got L, Sarda P, Roques J, Garrido F (2017) Influence of vacancy damage on He diffusion in apatite, investigated at atomic to mineralogical scales. Geochim Cosmochim Acta 197:87–103

Ginster U, Reiners PW, Nasdala L, Chanmuang NC (2019) Annealing kinetics of radiation damage in zircon. Geochim Cosmochim Acta 249:225–246

Gleadow AJW (2002) Fission track dating methods: principles and techniques, 4th edn. The University of Melbourne, pp 1–83

Gleadow AJW, Duddy IR, Green PF, Hegarty KA (1986) Fission track lengths in the apatite annealing zone and the interpretation of mixed ages. Earth Planet Sci Lett 78:245–254

Gleadow AJW, Hurford AJ, Quaife RD (1976) Fission track dating of zircon: improved etching techniques. Earth Planet Sci Lett 33:273–276

Green PF, Crowhurst PV, Duddy IR, Japsen P, Holford SP (2006) Conflicting (U–Th)/He and fission track ages in apatite: enhanced He retention, not anomalous annealing behaviour. Earth Planet Sci Lett 250(3–4):407–427

Guo TL (2004) Meso-Cenozoic Tectono-thermal History of Shiwandashan Basin, South China. Ph.D. Theses, Tongji University (Shanghao), pp. 1–114. (**in Chinese with English abstract**)

Hasebe N, Barbarand J, Jarvis K, Carter A (2004) Apatite fission-track chronometry using laser ablation ICP-MS. Chem Geol 207(3–4):135–145

Hendriks B, Redfield TF (2005) Apatite fission track and (U-Th)/He data from fennoscandia: an example of underestimation of fission track annealing in apatite. Earth Planet Sci Lett 236(1–2):443–458

Ho KS, Chen JC, Lo CH, Zhao HL (2003) ^{40}Ar–^{39}Ar dating and geochemical characteristics of Late Cenozoic basaltic rocks from the Zhejiang-Fujian region, SE China: eruption ages, magma evolution and petrogenesis. Chem Geol 197:287–318

Jiang WC, Li H, Evans NJ, Wu JH (2019) Zircon records multiple magmatic-hydrothermal processes at the giant Shizhuyuan W-Sn-Mo-Bi polymetallic deposit, South China. Ore Geol Rev 115:103160

Kasuya M, Naeser CW (1988) The effect of α-damage on fission-track annealing in zircon. Nucl Tracks Radiat Meas 14(4):477–480

Kesler SE, Wilkinson BH (2006) The role of exhumation in the temporal distribution of ore deposit. Econ Geol 101(5):919–922

Ketcham RA (2005) Forward and inverse modeling of low-temperature thermochronometry data. Rev Miner Geochem 58(1):275–314

Ketcham RA, Carter A, Donelick RA, Barbarand J, Hurford AJ (2007) Improved modeling of fission-track annealing in apatite. Am Miner 92(5–6):799–810

Ketcham RA, Gautheron C, Tassan-Got L (2011) Accounting for long alpha-particle stopping distances in (U–Th–Sm)/He geochronology: refinement of the baseline case. Geochim Cosmochim Acta 75(24):7779–7791

Lei DL (2020) Rb-Sr isotopic age of quartz fluid inclusions of Yingshan silver deposit in Tuorong County, Fujian province and its geological significance. Geol Fujian 39(01):1–10 (**in Chinese with English abstract**)

Lepvrier C, Maluski H, Tich VV, Leyreloup A, Thi PT, Vuong VN (2004) The Early Triassic Indosinian orogeny in Vietnam (Truong Son Belt and Kontum Massif); implications for the geodynamic evolution of Indochina. Tectonophysics 393(1–4):87–118

Li CH, Jiang YH, Xing GF, Guo KY, Li C, Yu MG, Zhao P, Wang Z (2015) Two periods of skarn mineralization in Baizhangyan W-Mo deposit, Southern Anhui province, Southeast China: evidence from zircon U-Pb and molybdenite Re–Os and sulfur isotope data. Resour Geol 65(3):193–209

Li HQ, Wang DH, Lu YF, Yang HM, Xu JX, Zhang JQ (2007) Rock-forming and ore-forming ages of the Yanbei Porphyry tin deposit in Jiangxi Province and their geological significance. Acta Geosci Sin 05:456–461 (**in Chinese with English abstract**)

Li J, Shi W, Zhang YQ, Dong SW (2016) Thermal evolution of the Hengshan extensional dome in central South China and its tectonic implications: new insights into low-angle detachment formation. Gondwana Res 35:425–441

Li SB (2017) Meo-Cenozoic tectonothermal pattern of the South China Block: constraints from the fission track analysis. Ph.D. Theses, Sun Yat-Sen University (Guangzhou), pp. 1–161. (**in Chinese with English abstract**)

Li SG (2004) Exhumation mechanism of the ultrahigh-pressure metamorphic rocks in Dabie mountains and continental collision process between the North and South China blocks. Earth Sci Front 03:63–70

Li SM, Xiao YP, Wang Q, Zhang XH, Yang L, Wang YL, Zhang CM (2013) Re-Os dating of molybdenite from the Tongcun Porphyry molybdenum deposit in Western Zhejiang province and its geological implications. Geol Explor 49(01):50–57 (**in Chinese with English abstract**)

Li XM, Wang YJ, Tan KX, Peng TP (2005) Meso-Cenozoic uplift and denudation of Yunkai block: constraints by fission track study. Chin Sci Bull 06:577–583 (**in Chinese with English abstract**)

Li QW, Zhao JH (2020) Amalgamation between the Yangtze and Cathaysia blocks in South China: evidence from the ophiolite geochemistry. Precambrian Res 350:105893

Li Y, Yuan F, Jowitt SM, Wang FY, Li XL, Deng YF, Wang YY, Zhou TF (2020) Molybdenite Re–Os, titanite and garnet U-Pb dating of the Magushan skarn Cu–Mo deposit, Xuancheng district, Middle-Lower Yangtze river metallogenic belt. Geosci Front 12(3):101116

Li ZX, Li XH, Wartho JA, Clark C, Li WX, Zhang CL, Bao CM (2010) Magmatic and metamorphic events during the early Paleozoic Wuyi-Yunkai orogeny, southeastern South China: new age constraints and pressure-temperature conditions. Geol Soc Am Bull 122(5–6):772–793

Liu GX, Deng YF, Yuan F, Chen XJ, Yang B (2021) Rb–Sr dating and S-Sr–Nd isotopic constraints on the genesis of the Hehuashan Pb–Zn deposit in the Middle-Lower Yangtze River Metallogenic belt, China. Solid Earth Sci. https://doi.org/10.1016/J.SESCI.2021.04.003

Liu SB, Liu ZQ, Wang CH, Wang DH, Zhao Z, Hu ZH (2017) Geochemical characteristics of REEs and trace elements and

Sm-Nd dating of scheelite from the Zhuxi giant tungsten deposit in northeast Jiangxi. Earth Sci Front 24(05):17–30 (**in Chinese with English abstract**)

Liu SS, Weber U, Glasmacher UA, Xu ZQ, Wagner GA (2009) Fission track analysis and thermotectonic history of the main borehole of the Chinese continental scientific drilling project. Tectonophysics 475(2):318–326

Liu WH, Zhang J, Li WT, Sun T, Jiang MR, Wang J, Wu JY, Chen CJ (2012) Metallogenic depth, post-mineralization uplift and denudation of porphyry-like type Iron deposits in Ningwu, Luzong basins: evidences from apatite fission track. Earth Sci 37(05):966–980 (**in Chinese with English abstract**)

Liu X, Fan HR, Evans NJ, Batt GE, McInnes IA, Yang KF, Qin KZ (2014) Cooling and exhumation of the mid-Jurassic porphyry copper systems in Dexing City, SE China: insights from geo-and thermochronology. Miner Depos 49(7):809–819

Mao JW, Cheng YB, Chen MH, Franco P (2013a) Major types and time–space distribution of Mesozoic ore deposits in South China and their geodynamic settings. Miner Depos 48:267–294

Mao JW, Xie GQ, Guo CL, Yuan SD, Cheng YB, Chen YC (2008) Spatial-temporal distribution of Mesozoic ore deposits in South China and their metallogenic settings. Geol J China Univ 14(04):510–526 (**in Chinese with English abstract**)

Mao JW, Xiong BK, Liu J, Pirajno F, Cheng YB, Ye HS, Song SW, Dai P (2017) Molybdenite Re/Os dating, zircon U-Pb age and geochemistry of granitoids in the Yangchuling porphyry W-Mo deposit (Jiangnan tungsten ore belt), China: implications for petrogenesis, mineralization and geodynamic setting. Lithos 286:35–52

Mao ZH, Cheng YB, Liu JJ, Yuan SD, Wu SH, Xiang XK, Luo XH (2013b) Geology and molybdenite Re–Os age of the Dahutang granite-related veinlets-disseminated tungsten ore field in the Jiangxin Province, China. Ore Geol Rev 53(3):422–433

Márton I, Moritz R, Spikings R (2010) Application of low-temperature thermochronology to hydrothermal ore deposits: formation, preservation and exhumation of epithermal gold systems from the eastern rhodopes, bulgaria. Tectonophysics 483(3–4):240–254

McDannell KT, Issler DR, O'Sullivan PB (2019) Radiation-enhanced fission track annealing revisited and consequences for apatite thermochronometry. Geochim Cosmochim Acta 252:213–239

Min K, Gao JF, Qi YQ, Liu Y, Yang SG (2020) Application of LA-ICP-MS/FT in the perservation of ore deposits—case studies of the Dexing Copper deposit and Yinshan Pb-Zn deposit, Northeastern Jiangxi Province. Geotecton Metallog 44(01):80–91 (**in Chinese with English abstract**)

Nancy DN, Charles WN (1984) Fission-track dating. Dev Palaeontol Stratigr 7:87–100

Nasdala L, Hanchar JM, Kronz A, Whitehouse MJ (2005) Long-term stability of alpha particle damage in natural zircon. Chem Geol 220(1):83–103

Nie LQ, Zhou TF, Fan Y, Zhang QM, Zhang M, Wang LH (2016) LA-ICPMS U-Pb zircon age and molybdenite Re-Os dating of Donggushan, the first tungsten deposit found in the Luzong orefield, Middle-Lower Yangtze River Valley Metallogenic Belt. Acta Petrol Sin 32(02):303–318 (**in Chinese with English abstract**)

Peng HQ, Jia BH, Tang XS (2004) Uplift process of Mufushan and thermochronology of Wangxiang granites in northeastern Hunan province. Bull Geol Sci Technol 01:11–15 (**in Chinese with English abstract**)

Pickering J, Matthews W, Enkelmann E, Guest B, Koblinger BM (2020) Laser ablation (U–Th)/He dating of detrital apatite. Chem Geol 548:119683

Price PB, Walker RM (1963) Fossil tracks of charged particles in mica and the age of minerals. J Geophys Res 68(16):4847–4862

Price PB, Walker RL (1962) Observation of charged-particle tracks insolids. J Appl Phys 33:3400–3406

Shen CB, Mei LF, Min K, Jonckheere R, Ratschbacher L, Yang Z, Peng L, Liu ZQ (2012) Multi-chronometric dating of the Huarong granitoids from the middle Yangtze Craton: implications for the tectonic evolution of eastern China. J Asian Earth Sci 52:73–87

Shi HC, Shi XY, Yang XQ, Jiang HY (2013) The exhumation process of Mufushan granite in Jiangnan uplift since Cenozoic: evidence from low-temperature thermochronology. Chin J Geophys 56(6):1945–1957 (**in Chinese with English abstract**)

Su QW, Mao JW, Wu SH, Zhang ZC (2017) Geochronology and geochemistry of the granitoids and ore—forming age in the Xiaoyao tungsten polymetallic skarn deposit in the Jiangnan Massif tungsten belt, China: implications for their petrogenesis, geodynamic setting, and mineralization. Lithos 296–299:365–381

Sun P, Guo PY, Niu YL (2021) Eastern China continental lithosphere thinning is a consequence of paleo-Pacific plate subduction: a review and new perspectives. Earth Sci Rev 218:103680

Sun T (2006) A new map showing the distribution of granites in South China and its explanatory notes. Geol Bull China 25(3):332–335 (**in Chinese with English abstract**)

Tagami T, Carter A, Furford AJ (1996) Natural long-term annealing of the zircon fission-track system in Vienna Basin deep borehole samples: constraints upon the partial annealing zone and closure temperature. Chem Geol 130:147–157

Tagami T, Ito H, Nishimura S (1990) Thermal annealing characteristics of spontaneous fission tracks in zircon. Chem Geol Isot Geosci 80(2):159–169

Tamer MT, Ketcham RA (2020) The along-track etching structure of fission tracks in apatite: observation and implications. Chem Geol 553:119809

Tang C, Yang X, Cao J (2019) Genesis of the Shangjinshan W-Mo polymetallic deposit in the Eastern Jiangnan tungsten belt: evidences from geochemistry, geochronology and zircon Hf isotope analyses. Ore Geol Rev 115:103172

Tang DLK, Seward D, Wilson CJN, Sewell RJ, Carter A, Paul BT (2014a) Thermotectonic history of SE China since the Late Mesozoic: insights from detailed thermochronological studies of Hong Kong. J Geol Soc Lond 171:591–604

Tang SL, Yan DP, Qiu L, Gao JF, Wang CL (2014b) Partitioning of the Cretaceous Pan-Yangtze basin in the central South China block by exhumation of the Xuefeng Mountains during a transition from extensional to compressional tectonics. Gondwana Res 25:1644–1659

Tao N, Li ZX, Danišík M, Evans NJ, Batt GE, Li WX, Pang CJ, Jourdan F, Xu YG, Liu YP (2017) Thermochronological record of Middle-Late Jurassic magmatic reheating to Eocene rift-related rapid cooling in the SE South China block. Gondwana Res 46:191–203

Tao N, Li ZX, Danišík M, Evans NJ, Li RX, Pang CJ, Li WX, Jourdon F, Yu Q, Liu LP, Batt GE, Xu YG (2019) Post-250 Ma thermal evolution of the central Cathaysia Block (SE China) in response to flat-slab subduction at the proto-Western Pacific margin. Gondwana Res 75:1–15

Vermeesch P (2017) Statistics for LA-ICP-MS based fission track dating. Chem Geol 456:19–27

Wan GL (2013a) Hunan Qianlishan Granite constraints on mineralization. Ph.D. Theses, China University of Geosciences (Beijing), pp 3–122 (**in Chinese with English abstract**)

Wan TF (2013b) A new Asian tectonic unit map. Geol China 40(05):1351–1365 (in Chinese with English abstract)

Wang F, Chen HL, Batt GE, Lin XB, Gong JF, Gong GH, Meng LF, Yang SF, Jourdon F (2015) Tectonothermal history of the NE Jiangshan-Shaoxing suture zone: evidence from $^{40}Ar/^{39}Ar$ and fission-track thermochronology in the Chencai region. Precambrain Res 264:192–203

Wang GG, Ni P, Zhao KD, Wang XL, Liu JQ, Jiang SY, Chen Y (2012) Petrogenesis of the middle Jurassic Yinshan volcanic-intrusive complex, SE China: implications for tectonic evolution and Cu-Au mineralization. Lithos 150:135–154

Wang XY, Suo YH, Li SZ, Cao XZ, Li XY, Zhou J, Wang PC, Jin C (2020a) Cenozoic uplift history and its dynamic mechanism along the eastern continental margin of South China. Acta Petrol Sin 36(6):1803–1820 (**in Chinese with English abstract**)

Wang Y, Deng JF, Wang JY, Xiong LP (2001) Terrestrial heat flow pattern and thermo-tectonic domains in the continental area of China. J Grad Sch Acad Sin 18(01):51–58 (**in Chinese with English abstract**)

Wang YF, Yang MH, Zhang LG, Lu SS, Yang ZF, Qiu XF, Dong ZP (2017) Metallogenic epoch and ore-forming material source of the Tongshanling Pb-Zn polymetallic deposit in southeastern Hu'nan Province: evidence from Sm-ND isochron age and Pb isotope. Geol Bull China 36(05):875–884 (**in Chinese with English abstract**)

Wang YN, Zhang J, Zhang BH, Zhao H (2018) Cenozoic exhumation history of South China: a case study from the Xuefeng Mt. Range J Asian Earth Sci 151:173–189

Wang YS, Bai Q, Tian ZQ, Lu SM, Li JS, Zhou YZ, Du H, Jiang C (2021) Exhumation history of late Mesozoic intrusions in the Tongling-Xuancheng area of the Lower Yangtze region, eastern China: evidence from zircon (U–Th)/He and apatite fission track thermochronology. Ore Geol Rev 135:104220

Wang Y, Wang YJ, Li SB, Seagren E, Zhang YZ, Zhang PZ, Qian X (2020b) Exhumation and landscape evolution in eastern South China since the Cretaceous: new insights from fission-track thermochronology. J Asian Earth Sci 191:104239

Wolfe MR, Stockli DF (2010) Zircon (U–Th)He thermochronometry in the KTB drill hole, germany, and its implications for bulk he diffusion kinetics in zircon. Earth Planet Sci Lett 295:69–82

Wu ZL (2021) Metallogenic age of Jinkeng gold polymetallic deposit in Shaowu City, Fujian Province. Miner Depos 40(01):19–33 (**in Chinese with English abstract**)

Wyborn LAI, Heinrich CA, Jaques AL (1994) Australian proterozoic mineral systems: essential ingredients and mappable criteria. In: Hallenstein PC (ed) Australian mining looks north-the challenges and choices, vol 5. Australian Institute of Mining and Metallurgy Publication Series, pp 109–115

Xi WW, Chen SZ, Zhu XT (2020) Research and discussion on the metallogenic epochs of the Xiashan Pb-Zn deposit in Zhenghe County, Fujian Province. Geol China 47(02):440–449 (**in Chinese with English abstract**)

Xia B, Liu LW, Li J, Lin XG, Xu LF, Lin LZ (2010) Metallogenic geochronology of Yuanzhuding Cu-Mo deposit in western Guangdong-eastern Guangxi metallogenic belt and its geological significance. Miner Depos 29(03):395–404 (**in Chinese with English abstract**)

Xiao F, Fan FP, Xing GF, Jiang SY (2021) Ore genesis of Qingyunshan Cu-Au deposit in the Dehua-Youxi area of Fujian Province, southeastern China: constraints from U-Pb and Re-Os geochronology, fluid inclusions, and H-O-S-Pb isotope data. Ore Geol Rev 132:104006

Xiao QL, Zhou TF, Hollings P, Wang SW, Liu J, Yang QG, Yuan F (2020) Mineral and whole-rock chemistry of the Chating porphyry Cu–Au deposit related intrusions in the Middle-Lower Yangtze River Belt, Eastern China: implications for magma evolution and mineralization. Lithos 380–381:105881

Xiao X, Zhou TF, Yuan F, Fan Y, Zhang DY, Liu DZ, Huang WP, Chen XF (2017) The geochronology of the Qingyang Gaojiabang tungsten-molybdenum deposit and its geological significance, Anhui Province, East China. Acta Petrol Sin 33(03):859–872 (**in Chinese with English abstract**)

Xie JC, Tang DW, Xia DM, Wang Y, Li QZ, Yang XY, Sun WD (2019) Geochronological and geochemical constraints on the formation of Chizhou Cu-Mo polymetallic deposits, middle and lower Yangtze metallogenic belt, eastern China. Ore Geol Rev 109:322–347

Xu YM, Jiang SY, Zhu JX (2021) Factors controlling the formation of large porphyry Cu deposits: a case study from the Jiurui ore district of Middle-Lower Yangtze River Metallogenic Belt using in situ zircon and apatite chemistry from syn-mineralization intrusions. Ore Geol Rev 2021:104082

Yamada R, Tagami T, Nishimura S, Ito H (1995) Annealing kinetics of fission tracks in zircon: an experimental study. Chem Geol 122(1–4):249–258

Yi Y, Carter A, Xia B, Lin G, Brichau S, Hu XQ (2009) A fission-track and (U–Th)/He thermochronometric study of the northern margin of the South China Sea: an example of a complex passive margin. Tectonophysics 474(3–4):584–594

Yang MG, Wu FJ, Shong ZR, Lu SJ (2015) North Jiangxi: A geological window of South China. Acta Geol Sin 89(02):222–233 ((**in Chinese with English abstract**))

Yao JM, Hua RM, Qu WJ, Qi HW, Lin JF, Du AD (2007) Re-Os isotope dating of molybdenites in the Huangshaping Pb-Zn-W-Mo polymetallic deposit, Hunan Province, South China and its geological significance. Sci China Ser D Earth Sci 50:519–526

Ye TZ, Lv ZC, Pang ZS et al (2014) Metallogenic prognosis theories and methods in exploration areas: Pandect. Geologic Publishing House, Beijing, pp 70–76 (**in Chinese**)

Yin A, Harrison TM (2000) Geologic evolution of the Himalayan-Tibetan Orogen. Annu Rev Earth Planet Sci 28:211–280

Yuan SD, Mao JW, Zhao PL, Yuan YB (2018) Geochronology and petrogenesis of the Qibaoshan Cu-polymetallic deposit, northeastern Hunan Province: implications for the metal source and metallogenic evolution of the intracontinental Qinhang Cu-polymetallic belt, South China. Lithos 302–303:519–534

Yuan SD, Zhang DL, Shuang Y, Du AD, Qu WJ (2012) Re-Os dating of molybdenite from the Xintianling giant W-molybdenum deposit in southern Hunan Province, China and its geological implications. Acta Petrol Sin 28(01):27–38 (**in Chinese with English abstract**)

Yuan YS, Ma YS, Hu SB, Guo TL, Fu XY (2006) Present-day geothermal characteristics in South China. Chin J Geophys 49(4):1118–1126 (**in Chinese with English abstract**)

Zhai YS (1999) On the metallogenic system. Earth Sci Front 01:14–28 (**in Chinese with English abstract**)

Zhang D, Wu GG, Di YJ, Wang CM, Yao JM, Zhang YY, Lv LJ, Yuan Y, Shi JJ (2012) Geochronology of diagenesis and mineralization of the Luoyang iron deposit in Zhangping city, Fujian Province and its geological significance. Earth Sci J China Univ Geosci 37:1217–1231 (**in Chinese with English abstract**)

Zhang DQ, She HQ, Li DX, Feng CY (2003) The porphyry-epithermal metallogenic system in the Zijinshan. Acta Geol Sin 77:253–261 (**in Chinese with English abstract**)

Zhang J, Liu XX, Zeng Z, Li W, Peng LL, Hu HB, Cheng JW, Lu KX (2021) Age constraints on the genesis of the Changkeng tungsten deposit, Nanling region, South China. Ore Geol Rev 134:104134

Zhang JJ, Chen ZH, Wang DH, Chen ZY, Liu SB, Wang CH (2008) Geological characteristics and metallogenic epoch of the Xingluokeng tungsten deposit, Fujian Province. Geotecton Metallog 01:92–97 (**in Chinese with English abstract**)

Zhang QQ, Gao JF, Tang YW, Min K (2020) In-situ LA-ICP-MS U-Pb dating and trace element analyses of Wolframites from the Xingluokeng Tungsten deposit in Fujian Province, China. Bull Miner Petrol Geochem 39(06):1278–1291+1311. (**in Chinese with English abstract**)

Zhang WL, Hua RM, Wang RC, Chen PR, Li HM (2006) New dating of the Dajishan granite and related tungsten mineralization in Southern Jiangxi. Acta Geol Sin 07:956–962 (**in Chinese with English abstract**)

Zhao PL, Yuan SD, Mao JW, Santosh M, Li C, Hou KJ (2016) Geochronological and petrogeochemical constraints on the skarn deposits in Tongshanling ore district, southern Hunan Province: implications for Jurassic Cu and W metallogenic events in South China. Ore Geol Rev 78:120–137

Zhao XY, Zhong H, Mao W, Bai ZJ, Xue K (2020) Molybdenite Re-Os dating and LA-ICP-MS trace element study of sulfide minerals from the Zijinshan high-sulfidation epithermal Cu-Au deposit, Fujian Province, China. Ore Geol Rev 118:103363

Zheng Y, Yu XQ, Yuan WM, De EW, Jiang GB, Zhu DL, Wang C, Jia YY (2011) Exhumation history of the Huangshan granite pluton, southern Anhui Province: new insights from fission-track analysis. Sci China Earth Sci 54(4):528–539

Zhong J, Chen YJ, Pirajno F, Chen J, Li J, Qi JP, Li N (2014) Geology, geochronology, fluid inclusion and H-O isotope geochemistry of the Luoboling porphyry Cu–Mo deposit, Zijinshan Orefield, Fujian Province, China. Ore Geol Rev 57:61–77

Zhou TF, Wang SW, Fan Y, Yuan F, Zhang DY, White NC (2015) A review of the intracontinental porphyry deposits in the Middle-Lower Yangtze River Valley metallogenic belt, Eastern China. Ore Geol Rev 65:433–456

Zhou XM, Sun T, Shen WZ, Shu LS, Niu YL (2006) Petrogenesis of Mesozoic granitoids and volcanic rocks in South China: a response to tectonic evolution. Episodes 29(1):26–33

Zuo LY, Hou ZQ, Meng XJ, Yang ZM, Song YC, Li Z (2010) SHRIMP U-Pb zircon geochronology of the ore-bearing rock in the Lengshuikeng porphyry type Ag-Pb-Zn deposit. Geol China 37(05):1450–1456 (**in Chinese with English abstract**)

Zuo XR (2015) Active-passive margin transition in the Cathaysia Block: thermochronological and kinematic constraints. HKU Theses Online (HKUTO), pp 1–256